

# Detailed traveltimes tomography and seismic catalogue around the 2019 $M_w$ 7.1 Ridgecrest, California, earthquake using dense rapid-response seismic data

Malcolm C.A. White<sup>1b</sup>,<sup>1</sup> Hongjian Fang<sup>2b</sup>,<sup>2</sup> Rufus D. Catchings,<sup>3</sup> Mark R. Goldman,<sup>4</sup> Jamison H. Steidl<sup>5</sup> and Yehuda Ben-Zion<sup>1,6</sup>

<sup>1</sup>Department of Earth Sciences, University of Southern California, Los Angeles, CA, USA. E-mail: [malcolm.white@usc.edu](mailto:malcolm.white@usc.edu)

<sup>2</sup>Department of Earth, Atmospheric and Planetary Sciences, Massachusetts Institute of Technology, Cambridge, MA, USA

<sup>3</sup>Earthquake Hazards Program, United States Geological Survey, Menlo Park, CA, USA

<sup>4</sup>Earthquake Science Center, United States Geological Survey, Menlo Park, CA, USA

<sup>5</sup>Earth Research Institute, University of California Santa Barbara, Santa Barbara, CA, USA

<sup>6</sup>Southern California Earthquake Center, University of Southern California, Los Angeles, CA, USA

Accepted 2021 June 2. Received 2021 June 2; in original form 2020 December 15

## SUMMARY

We derive a detailed earthquake catalogue and  $V_p$ ,  $V_s$  and  $V_p/V_s$  models for the region around the 2019  $M_w$  6.4 and  $M_w$  7.1 Ridgecrest, California, earthquake sequence using data recorded by rapid-response, densely deployed sensors following the Ridgecrest main shock and the regional network. The new catalogue spans a 4-month period, starting on 1 June 2019, and it includes nearly 95 000 events detected and located with iterative updates to our velocity models. The final  $V_p$  and  $V_s$  models correlate well with surface geology in the top 4 km of the crust and spatial seismicity patterns at depth. Joint interpretation of the derived catalogue, velocity models, and surface geology suggests that (i) a compliant low-velocity zone near the Garlock Fault arrested the  $M_w$  7.1 rupture at the southeast end; (ii) a stiff high-velocity zone beneath the Coso Mountains acted as a strong barrier that arrested the rupture at the northwest end and (iii) isolated seismicity on the Garlock Fault accommodated transtensional-stepover strain triggered by the main events. The derived catalogue and velocity models can be useful for multiple future studies, including further analysis of seismicity patterns, derivations of accurate source properties (e.g. focal mechanisms) and simulations of earthquake processes and radiated seismic wavefields.

**Key words:** Body waves; Crustal imaging; Earthquake dynamics; Seismicity and tectonics; Seismic tomography; Dynamics and mechanics of faulting.

## 1 INTRODUCTION

On 4 July 2019, a  $M_w$  6.4 earthquake ruptured a previously unmapped fault near the town of Ridgecrest, California. Thirty-four hours later, a  $M_w$  7.1 earthquake ruptured another nearby unmapped fault during the largest earthquake to rattle southern California since the 1999  $M7.1$  Hector Mine earthquake. The earthquake science community responded quickly, and field teams led by the United States Geological Survey (USGS) and the Southern California Earthquake Center (SCEC) deployed 480 seismic sensors to record seismic data generated by the subsequent aftershock sequence (Steidl *et al.* 2019; Catchings *et al.* 2020; Cochran *et al.* 2020). The data collected by these sensors complement a wide array of additional *in situ* field observations (e.g. Brandenberg *et al.* 2020; DuRoss *et al.* 2020; Floyd *et al.* 2020; Mattioli *et al.* 2020; Ponti *et al.* 2020) and remote-sensing observations (e.g. Donnellan

*et al.* 2020; Fielding *et al.* 2020; Hudnut *et al.* 2020; Jin & Fialko 2020; Magen *et al.* 2020; Pierce *et al.* 2020) of various kinds. The results from these data highlighted the significant structural and earthquake complexities in the area.

Multiple studies have investigated details of the Ridgecrest earthquake sequence by examining spatiotemporal seismicity patterns observed in earthquake catalogues (e.g. Ross *et al.* 2019; Lee *et al.* 2020a,b; Lin 2020; Liu *et al.* 2020; Lomax 2020; Shelly 2020). Previous such analyses, however, only cover about 1 month of the aftershock sequence or less and do not include results based on the rapid-response dense deployment of seismographs. Although the standard earthquake catalogue for this region (Hauksson *et al.* 2012) offers extensive records of the Ridgecrest sequence, it also does not use the dense data that were collected in response to the  $M_w$  6.4 and  $M_w$  7.1 events. Furthermore, no study until now has combined fully 3-D procedures for locating earthquakes and up-

dating velocity models. To improve the information on seismicity patterns and crustal structures in the region around the Ridgecrest earthquake sequence, in this study, we derive a local earthquake catalogue and velocity models ( $V_p$ ,  $V_s$  and  $V_p/V_s$ ) using rapid-response dense-deployment seismic data and data from the SCSN. The obtained new catalogue has roughly 95 000 earthquakes covering 1 month of foreshocks and 3 months of the aftershock sequence and is used to perform detailed traveltimes tomography analysis for seismic velocity structures in the area.

To derive an earthquake catalogue that is independent of *a priori* observations, we processed raw waveform data recorded by 152 seismic sensors over a 4-month period, starting 1 month before the main shocks, using an automated processing procedure. We then iteratively updated event locations and velocity models using fully 3-D methods based on the fast marching method for solving the eikonal equation (Fang *et al.* 2020; White *et al.* 2020). Joint interpretation of the derived seismicity and  $V_p$ ,  $V_s$  and  $V_p/V_s$  models, along with the surface geology, suggests that (i) compliant crust associated with the Garlock Fault arrested rupture of the  $M_w$  7.1 event propagating to the southeast; (ii) rigid crust beneath the Coso Mountains acted as a strong barrier that arrested the rupture propagation to the northwest and (iii) isolated seismicity on the Garlock Fault accommodated transtensional-stepover strain triggered by the main events.

The data used in this paper are described in Section 2. A general description of the processing procedure is provided in Section 3, and more detailed technical material is presented in the Appendix. The main results obtained are presented in Section 4, and we discuss our interpretation of the results in Section 5. The derived seismic catalogue and velocity models can be useful for multiple future studies in the region.

## 2 DATA

Rapid response teams, led by the USGS and SCEC, started progressively deploying 480 seismic sensors in the region surrounding the  $M_w$  6.4 and  $M_w$  7.1 earthquakes on 7 July (Steidl *et al.* 2019; Catchings *et al.* 2020; Cochran *et al.* 2020). The network codes assigned by the International Federation for Digital Seismograph Networks (FDSN) to these deployments are **3J** (Steidl *et al.* 2019), **GS** (Albuquerque Seismological Laboratory & United States Geological Survey 1980) and **ZY** (California Institute of Technology & United States Geological Survey 1926). Data from the 3J network are accessible through the Incorporated Research Institutions for Seismology Data Management Center (IRIS DMC), data from the ZY network are available through the Southern California Earthquake Data Center (SCEDC; Southern California Earthquake Center 2013) and data from the GS network are available through both the IRIS DMC and the SCEDC.

The 3J network comprises 461 three-component (3C) nodal seismometers, deployed in 14 subarrays. Two subarrays form rectangular grids, 11 form fault-perpendicular linear arrays and the remaining one is a sparse array of three nodal seismometers that were collocated with broad-band seismometers. In this study, we use data from the two rectangular grids (Fig. 1). 47 nodal seismometers, centred on the main shock ruptures, operating between 14 July and 10 September, and deployed with nominal interstation spacing of 10 km, make up the first such array, which we herein refer to as 3J.R. 31 nodal seismometers, centred on an isolated swarm of seismicity on the Garlock Fault to the southwest of the main shocks, operating between 8 August and 10 September, and deployed with nominal

inter-station spacing of 5 km, make up the second rectangular array, which we herein refer to as 3J.G. All data from the 3J.R and 3J.G arrays were sampled at  $500 \text{ s}^{-1}$  (see Catchings *et al.* 2020, for details).

The GS network added 10 new stations (Cochran *et al.* 2020), which began recording as early as 7 July 2019. All 10 sites were occupied by strong-motion accelerometers, and six sites were collocated with broad-band seismometers. In this study, we use data from the six broad-band seismometers, all of which were sampled at  $100 \text{ s}^{-1}$ .

The ZY network added nine stations (Cochran *et al.* 2020), each with a collocated broad-band seismometer and strong-motion accelerometer, which also began recording as early as 7 July 2019. Here, we use data from all nine broad-band seismometers, which were sampled at  $100 \text{ s}^{-1}$  for all but one seismometer, which was sampled at  $200 \text{ s}^{-1}$ .

The permanent regional network, operated by Caltech and assigned the CI network code (California Institute of Technology & United States Geological Survey 1926; Southern California Earthquake Center 2013), provides continuity of data coverage before and after the rapid-response deployments, along with a coarse regional coverage of our study area. In this study, we use data from 55 stations maintained by the CI network, plus three stations contributed by the Nevada Seismic Network (network code NN; University of Nevada Reno 1971), and one station contributed by the Southern Great Basin Network (network code SN; University of Nevada Reno 1980). All data from the permanent regional network are recorded by broad-band seismometers and are archived with a uniform sample rate of  $100 \text{ s}^{-1}$  at the SCEDC.

During the procedure for associating detected phase arrivals with earthquake sources, we use a 1-D velocity model based on the model of Zhang & Lin (2014). We derive updated velocity models from traveltimes tomography for various initial models, including the SCEC Community Velocity Model (CVM) version H15.1 (CVMH; Shaw *et al.* 2015), SCEC CVM version S4.26 (CVMS; Lee *et al.* 2014), Modified Hadley-Kanamori 1-D model (HK1D; Hauksson 2000) and a regional model in development (FANG3D), derived using phase arrivals downloaded from the SCEDC and the same traveltimes tomography method used here. We use the HK1D model as a starting model instead of the 1-D model used for associating phase arrivals to test model robustness by starting with a reasonable model with minimal *a priori* information about local structure. Data for CVMH, CVMS and HK1D were extracted using the SCEC Unified Community Velocity Model software (Small *et al.* 2017).

## 3 METHODS

In this section, we describe key elements of the workflow used to derive an earthquake catalogue and tomographic models from raw waveform data, proceeding through each processing step in order.

### 3.1 Detecting earthquakes and measuring phase arrival times

Detecting earthquakes in continuous waveform data is the first critical procedure in our automated workflow, and this problem is intricately connected to that of measuring the arrival times of seismic phases ( $P$  and  $S$  waves); we treat the two problems in tandem. The description that follows is conceptual, and the reader is referred to the Appendix for a detailed technical explanation.

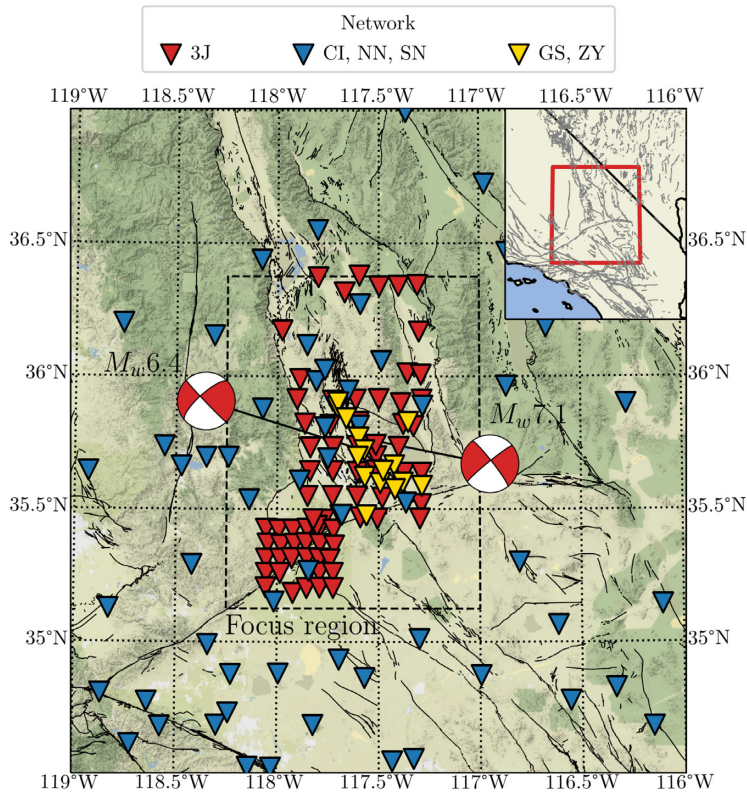


**Figure 1.** Map of stations used in this study, colour coded by FDSN network code. Data from rapid-response deployments used in this study include fifteen broad-band seismometers (GS and ZY networks; gold triangles) and 78 nodal seismometers (3J network; red triangles). An additional 55 permanent broad-band stations (CI, NN and SN networks; blue triangles) provide regional coverage of the study area. Beach balls show focal mechanisms of  $M_w$  6.4 and  $M_w$  7.1 main shocks, as determined by the USGS. Solid black lines indicate Quaternary fault traces, and the black dashed line delineates the focus region targeted in this study.

**Table 1.** The number of Voronoi cells and aspect ratio used for each iteration of the velocity model update.

Iterations	# of Voronoi cells	Aspect ratio
1,2,3	64	1,4,8
4,5,6	128	1,4,8
7,8,9	256	1,4,8
10,11,12	512	1,4,8
13,14,15	1024	1,4,8

We detect earthquakes on a per-station basis by applying a dynamic threshold to a characteristic function derived from 3C waveform data that targets potential  $P$ -wave arrivals. We target  $P$  waves because they arrive first and are often clearer than the later arriving  $S$  waves, which can be obfuscated by coda from the preceding  $P$  wave. The characteristic function combines measures of signal energy (via the ratio of short- to long-term amplitude averages, or the STA/LTA), the signal kurtosis and the ratio of horizontally to vertically polarized energy. Our algorithm registers a candidate  $P$ -wave arrival whenever the characteristic function exceeds its own average over the preceding 5 s by a factor of 6 or more. After registering a candidate  $P$ -wave arrival, the algorithm measures its arrival time using the Akaike Information Criterion (AIC; Akaike 1974; Maeda 1985) to determine the sample that optimally divides a small window of data (1 s centred on the intersection of the characteristic function and threshold) into noise and signal segments. We process the entire data set in this way to obtain a comprehensive set of candidate  $P$ -wave arrivals.

After detecting potential  $P$  waves and measuring their arrival times throughout the entire data set, we probe seismograms during the time interval between successive pairs of  $P$ -wave arrivals for  $S$ -wave arrivals, assuming that at most one  $S$ -wave arrival exists between each successive pair of  $P$ -wave arrivals. Instead of detecting potential  $S$  waves and then measuring their arrival times, we reverse the procedure. Assuming that an  $S$ -wave exists, we estimate its arrival time using the AIC method and then perform retrospective tests to validate its authenticity, discarding the measurement if it fails these tests. These retrospective tests comprise a signal-to-noise ratio threshold and a horizontal-to-vertical amplitude ratio threshold.

### 3.2 Associating arrivals with earthquakes

Having detected and measured arrival times of potential  $P$  and  $S$  waves, we associate them with earthquake sources using the Rapid Earthquake Association and Location algorithm (REAL; Zhang *et al.* 2019) and the 1-D average profile of the 3-D velocity model for the Coso geothermal area from Zhang & Lin (2014). We test various algorithm parameters and find that our results are primarily sensitive to the threshold for the number of associated phases; in the final analysis, we retain only events associated with at least eight  $P$ -wave arrivals, four  $S$ -wave arrivals and 16 total arrivals ( $P$  and  $S$ ).

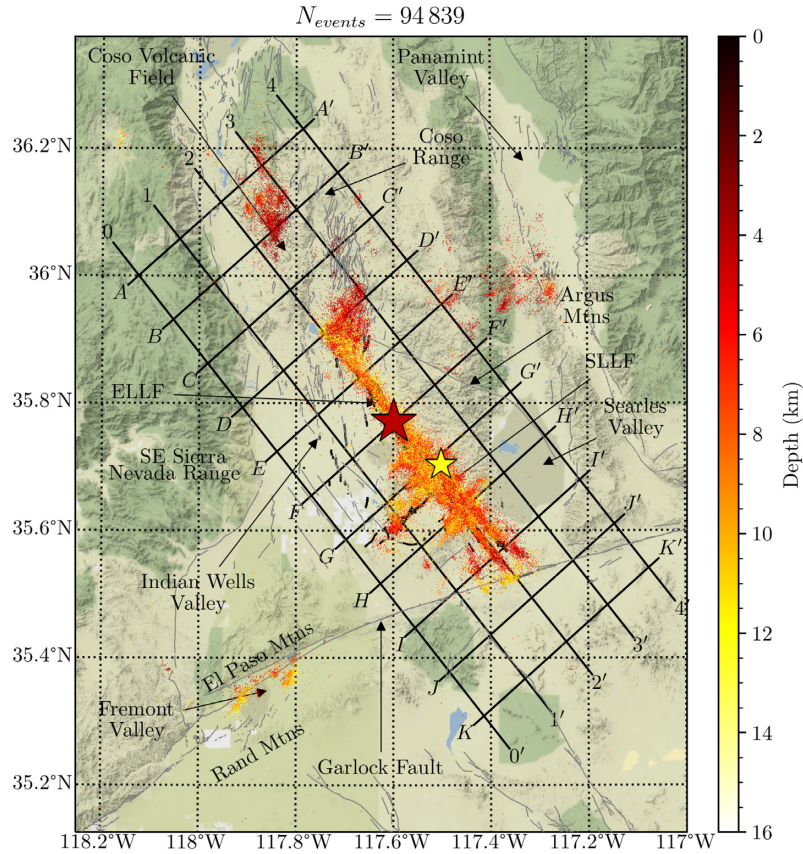


**Figure 2.** Seismicity map (events colour-coded by hypocentral depth) showing locations of 94 855 earthquakes located in this study. Solid black lines represent cross sections shown in Figs 11–15. Various geographical features are labeled, and the locations of the  $M_w$  6.4 and  $M_w$  7.1 main shocks (small yellow and large red star, respectively) are shown for reference.

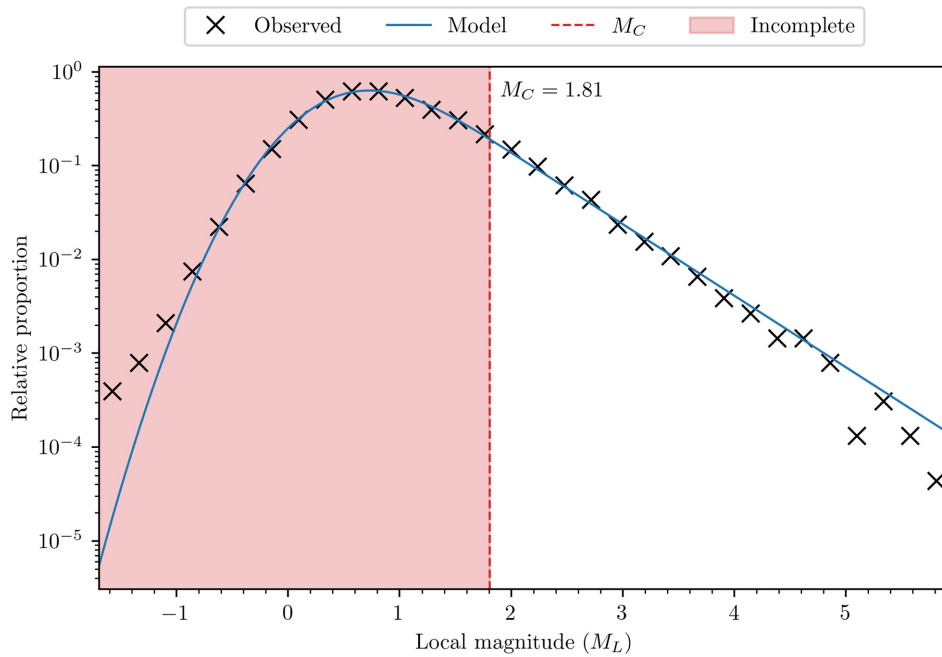


**Figure 3.** Observed (black crosses) and modeled (blue curve) frequency-magnitude distribution of the obtained catalogue. The vertical, dashed, red line marks the estimated magnitude of catalogue completeness,  $M_C$  and the shaded, red area indicates the incomplete portion of the catalogue.

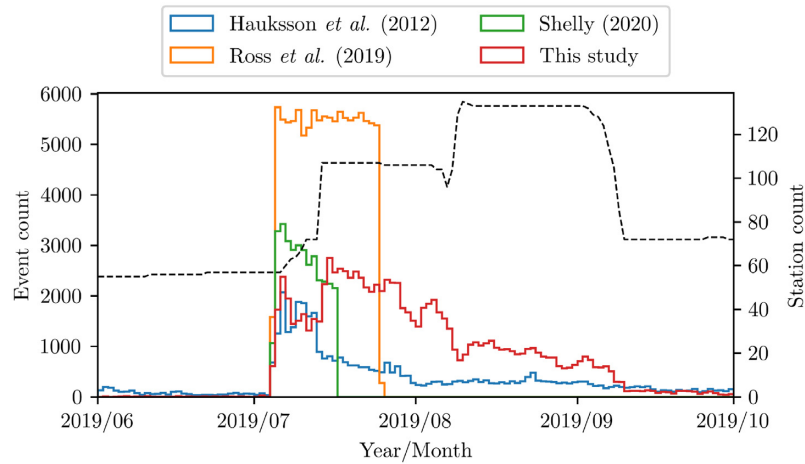


**Figure 4.** Number of events per day in the catalogues of the SCSN (Hauksson *et al.* (2012); blue curve), Ross *et al.* (2019; orange curve), Shelly (2020; green curve), and this study (red curve). Event counts are scaled according to the vertical axis on the left-hand side of the plot. Timeline of the number of stations used (black dashed line), scaled according to the vertical axis on the right-hand side of the plot.

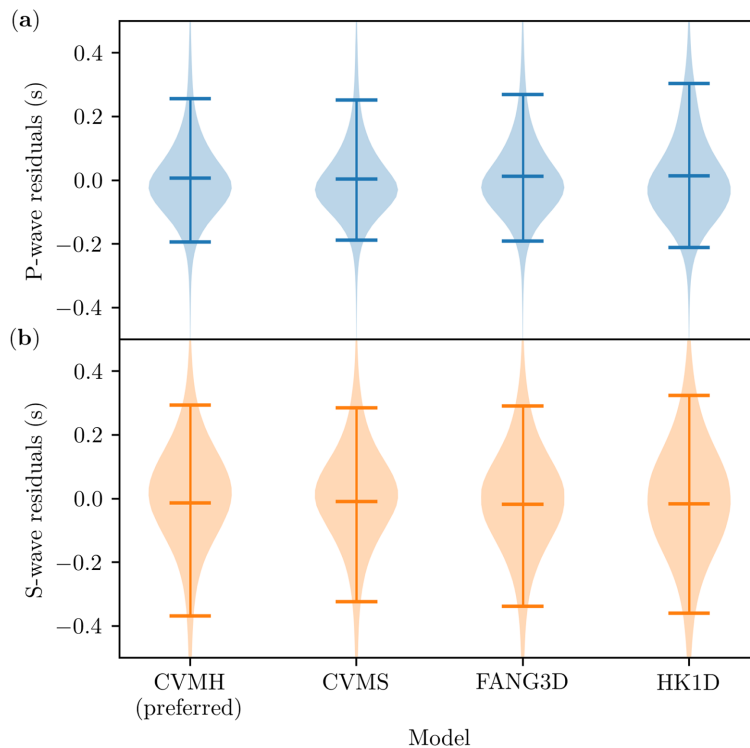


**Figure 5.** Final distribution of (a) *P*-wave and (b) *S*-wave arrival-time residuals for each of the initial models. The top, middle and bottom horizontal line for each distribution marks the 95th percentile, mean and 5th percentile, respectively.

### 3.3 Locating earthquakes

Earthquake hypocentres comprise four coordinates—three spatial and one temporal—which can be inferred from observed phase arrival times. We locate earthquakes by finding the hypocentre coordinates,  $\mathbf{h}_0$ , that minimize the  $\ell_2$ -norm of the residual vector between observed and synthetic phase arrival times. That is

$$\mathbf{h}_0 \equiv \arg \min_{\mathbf{h}} \|\mathbf{d} - \mathbf{p}(\mathbf{h})\|_2, \quad (1)$$

where  $\mathbf{d}$  and  $\mathbf{p}$  are vectors of observed and synthetic phase arrival times for a given event, respectively, and  $\mathbf{h}$  is an arbitrary hypocentre

four-vector. Determining  $\mathbf{h}_0$  for a given set of observations using eq. (1) requires two things: (i) a method to compute synthetic phase arrival times for an arbitrary hypocentre (the forward problem) and (ii) a method to search for  $\mathbf{h}_0$  in the space of possible values of  $\mathbf{h}$  (the inverse problem).

A convenient software for solving the forward problem is provided by PyKonal (White *et al.* 2020), which we use as a core computational engine for both locating earthquakes and updating the velocity model. Using PyKonal to compute  $\mathbf{p}(\mathbf{h})$ , we obtain an approximate solution to eq. (1) using the Differential Evolution

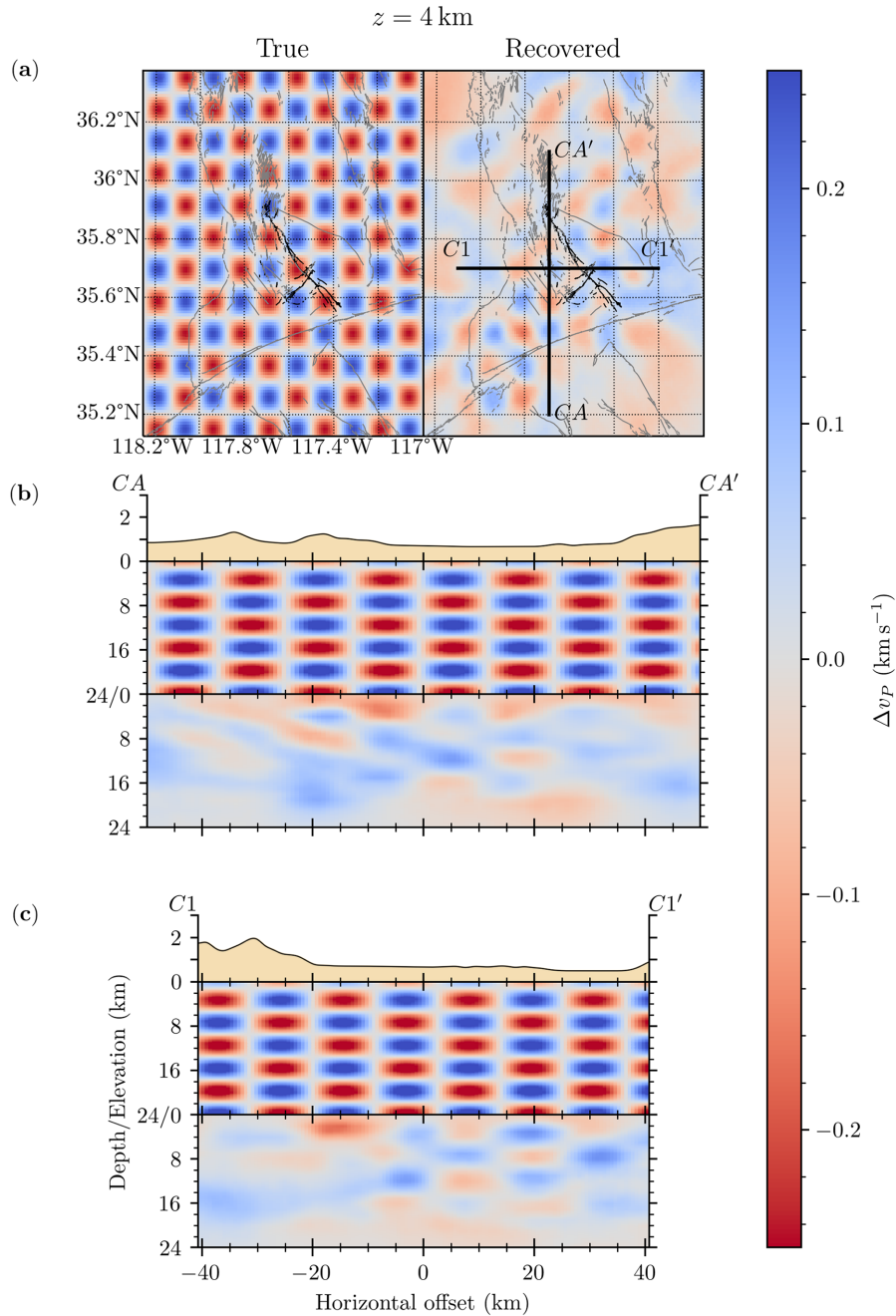


**Figure 6.** (a) Map view of a horizontal slice at 4 km depth through the true and recovered models of a checkerboard test for  $P$ -wave resolution. Thick, black lines show the surface traces of vertical transects (b)  $CA-CA'$  and (c)  $C1-C1'$ .

Optimization algorithm (Storn & Price 1997) implemented by the SciPy Python package (Virtanen *et al.* 2020).

### 3.4 Estimating local event magnitudes, $M_L$ and magnitude of catalogue completeness, $M_C$

To estimate the local magnitude,  $M_L$ , for each event, we measure maximum peak-to-peak  $S$ -wave amplitude on horizontal-component data with simulated Wood–Anderson response ( $A$  in eq. 2) and use the equations of Hutton & Boore (1987, their eqs 1 and 3) with no station corrections (i.e.  $S = 0$  in their eq. 1). That is, we compute the local magnitude from an individual amplitude measurement made on an instrument  $d$  kilometres from the event hypocentre as

$$M_L = \log_{10}(A) + 1.11 \cdot \log_{10}\left(\frac{d}{100}\right) + 0.00189 \cdot (d - 100) + 3. \quad (2)$$

We compute  $M_L$  for both horizontal components of every station that registered an  $S$ -wave arrival and report the median value as the event magnitude. We also report the median absolute deviation as a measure of uncertainty.

Following White *et al.* (2019), we estimate the magnitude of catalogue completeness,  $M_C$ , as the 99th percentile of the Gaussian component of an exponentially modified Gaussian probability

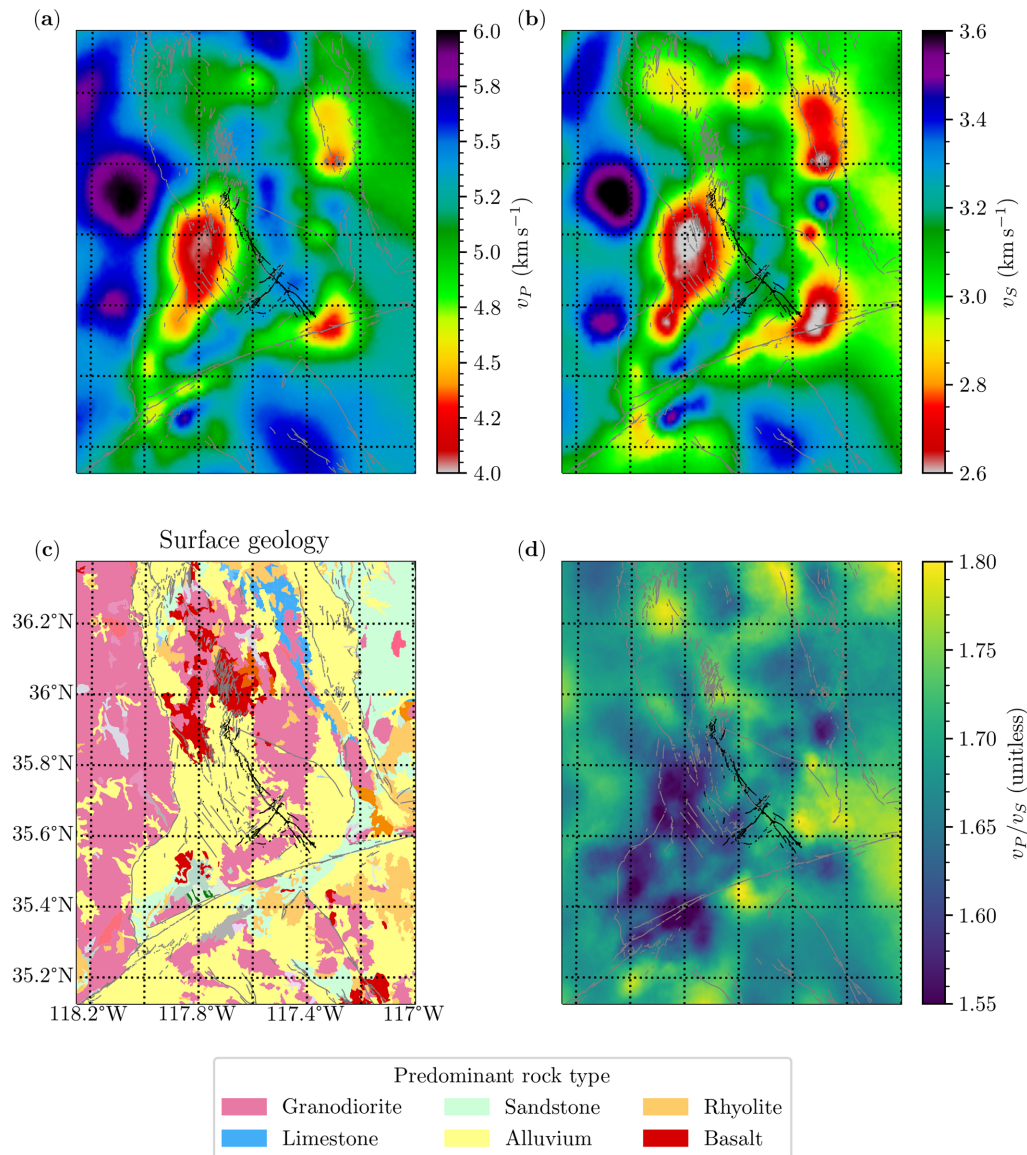


**Figure 7.** Horizontal slices of (a)  $P$ -wave velocity, (b)  $S$ -wave velocity, and (d)  $V_P/V_S$  ratio at 2 km below sea level, and (c) map of surface geology compiled by the USGS with legend below.

density function (pdf). That is, we model the observed frequency–magnitude distribution of the catalogue using eq. (3):

$$f_M(m; \mu, \sigma, \lambda) \equiv \lambda \exp\left(\frac{\lambda}{2}(2\mu + \lambda\sigma^2)\right) \times \exp(-\lambda m) \times \Phi\left(\frac{m - (\mu + \lambda\sigma^2)}{\sigma}\right), \quad (3)$$

in which  $\Phi$  is a Gaussian cumulative distribution function (cdf), and  $\mu$ ,  $\sigma$  and  $\lambda$  are model parameters estimated using maximum-likelihood estimation. The 99th percentile of the Gaussian pdf corresponding to  $\Phi$  is reported as the magnitude of catalogue completeness.

### 3.5 Traveltime tomography

Starting with an initial model (i.e. one of CVMH, CVMS, HK1D or FANG3D), we iteratively derive model updates via traveltime

tomography formulated using the method of Poisson-Voronoi subspace projections (Fang *et al.* 2020). This method is used here with three key changes: (i) cell centres are sampled randomly from a non-uniform distribution; (ii) cells are contracted along the vertical axis and (iii) arrival time observations are randomly sampled in proportion to non-uniform weights.

Drawing Voronoi cell centres from a non-uniform distribution permits model resolution to vary as the data allow and structures demand. To obtain variable model resolution, we distribute Voronoi cell centres vertically in proportion to the vertical velocity gradient and horizontally in proportion to the station density. To concentrate Voronoi cells where vertical velocity gradients are strongest (e.g. in the top few kilometres of the crust), their depth coordinates are drawn from a pdf defined by the smoothed gradient magnitude of the average 1-D velocity profile. To concentrate Voronoi cells where station coverage is densest, their horizontal coordinates are drawn from a pdf defined by the kernel density estimate for the station distribution with bandwidth determined using Scott's

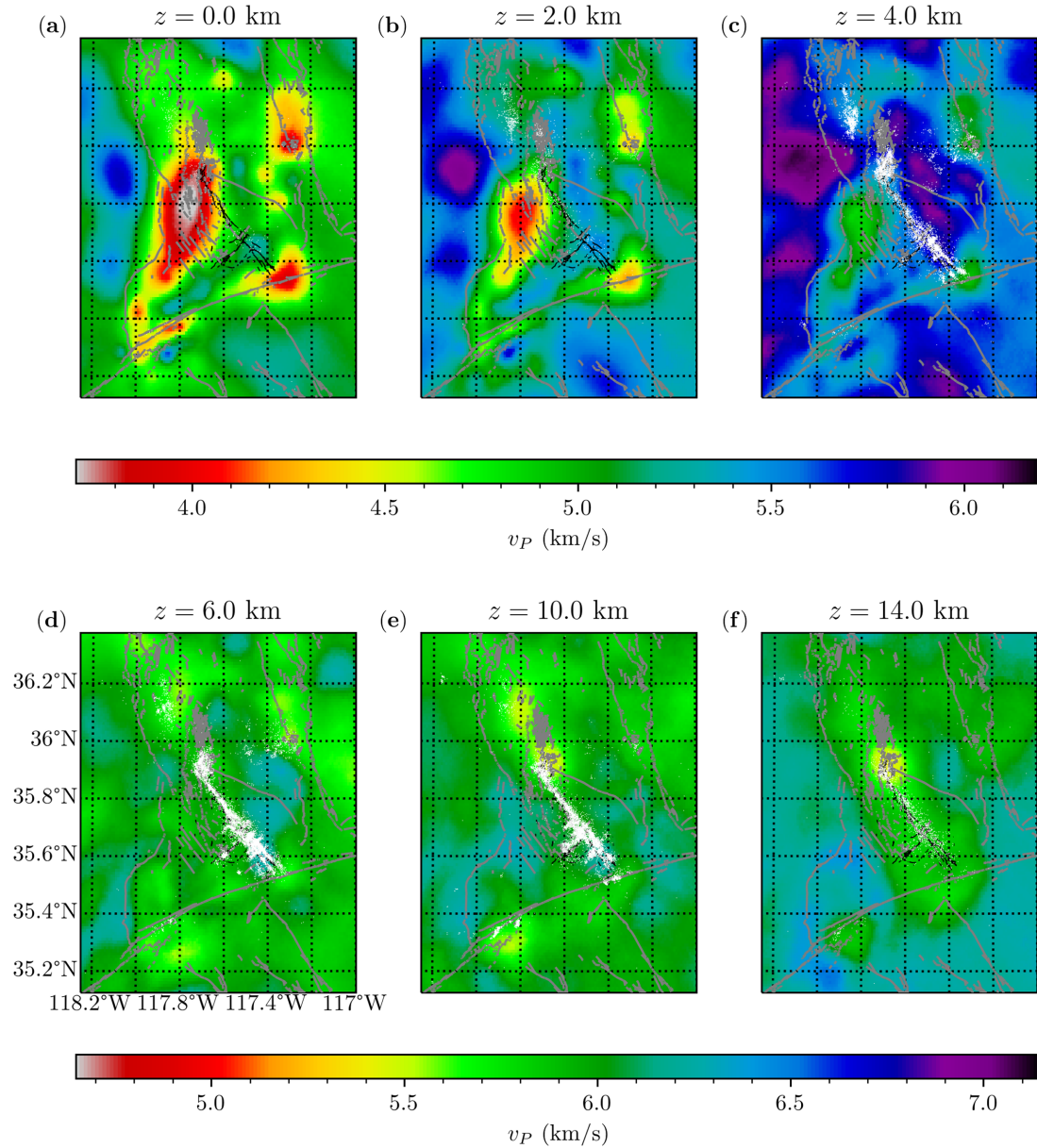


**Figure 8.** Horizontal slices through our  $V_p$  model at various depths (referenced relative to sea level). Panels in the top row are scaled according to the top colour bar, and panels in the second row are scaled according to the bottom colour bar. Seismicity within  $\pm 500$  m of each depth slice are shown as white dots.

rule (Scott 2015) as implemented in the SciPy Python package by `scipy.stats.gaussian_kde` (Virtanen *et al.* 2020). This automated choice of bandwidth effectively increased Voronoi-cell density beneath the 3J.R and 3J.G arrays without over-concentrating the cells beneath individual stations.

Neglecting discontinuities between lithologic units, we assume that vertical velocity gradients are larger than their horizontal counterparts, particularly in the top few kilometres of the crust, where the low confining pressure and surface processes enhance the generation of rock damage. To improve resolution of vertical velocity gradients, we deform Voronoi cells by compressing them along the vertical axis. Doing so increases the sensitivity of the inverse problem to vertical velocity gradients at the expense of decreased sensitivity to horizontal gradients. We define the *aspect ratio* of a Voronoi cell as the ratio of its vertical to horizontal dimensions (a high aspect ratio implies a flattened pancake-like Voronoi cell).

In the ideal case, ray paths sample the entire model space uniformly. In reality, however, ray coverage is strongly heterogeneous. Because our formulation of the tomographic inverse problem comprises multiple subproblems, each using a random subset of the observed data, we can sample the observations in a way that homogenizes ray coverage for each subproblem. To homogenize ray coverage, we sample observations in proportion to a weight that we assign each: that is  $w_i = e^{-P(\theta_i, \phi_i, z_i, \psi_i, \Delta_i)}$ , in which  $w_i$  is the weight assigned to the  $i$ th ray,  $\theta_i$ ,  $\phi_i$  and  $z_i$  are the latitude, longitude, and depth coordinates of the associated event, respectively,  $\psi_i$  and  $\Delta_i$  are the event-to-station azimuth and distance, respectively, and  $P(\cdot)$  is the joint pdf representing the probability of sampling an observation with the given parameters from the observed data set. We compute these weights using a 5-D kernel density estimate to estimate  $P(\cdot)$ , with all five coordinates normalized to lie in  $[0, 1]$ .

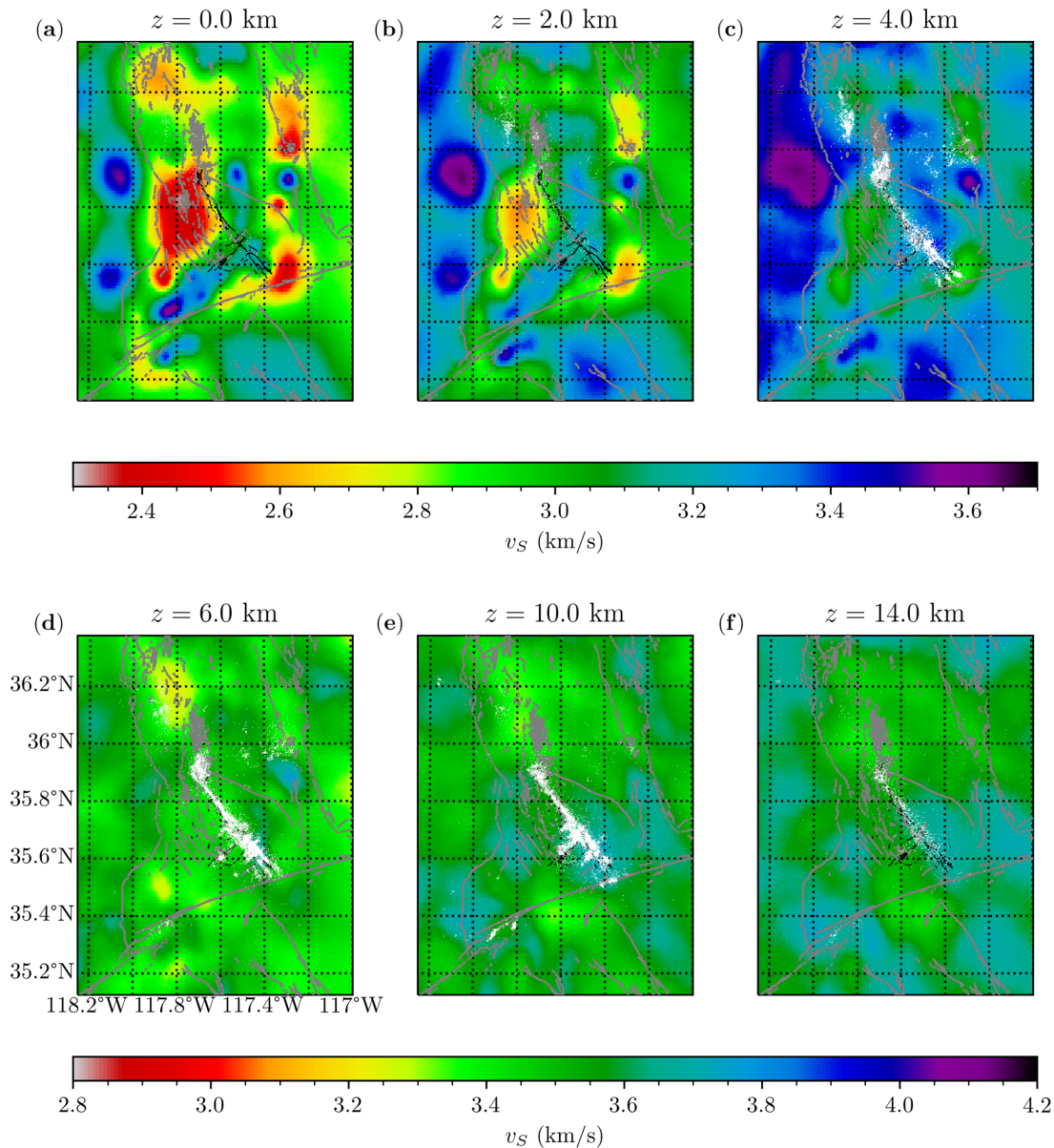


**Figure 9.** Horizontal slices through our  $V_s$  model, as discussed in Fig. 8.

1] and a bandwidth of 0.1. This choice of bandwidth for normalized data was empirically determined to effectively homogenize ray sampling.

With the algorithm of Fang *et al.* (2020) modified as described above, we iteratively refine the initial models by gradually increasing the number of Voronoi cells and cycling through a set of three aspect ratios (Table 1). The first three iterations use 64 Voronoi cells and an aspect ratio of 1 for the first iteration, 4 for the second and 8 for the third. The next three iterations double the number of Voronoi cells (128) and proceed through the same three aspect ratios (1, 4 and 8). We progressively double the number of Voronoi cells in this way until a maximum number of 1024 is reached. Each iteration comprises 128 random realizations for each phase ( $P$  and  $S$ ), and each random realization uses 32 648 randomly sampled observations, which helps mitigate biases due to differences between the number of observations for each phase (e.g. having more  $P$ - than  $S$ -wave observations). The median result is used to update the models at each iteration, and we relocate all events in the catalogue

using the updated model after each model update. We derive the  $V_p/V_s$  model by directly dividing the  $V_p$  model by the  $V_s$  at each grid node. Model uncertainties ( $\sigma_p$  and  $\sigma_s$  for the  $V_p$  and  $V_s$  models, respectively) are estimated by the standard deviation of the random realizations at each grid node and propagated to the  $V_p/V_s$  model via eq. (4):

$$\sigma_{P/S} = \sqrt{\left(\frac{\partial}{\partial V_p} \frac{V_p}{V_s}\right)^2 \sigma_p^2 + \left(\frac{\partial}{\partial V_s} \frac{V_p}{V_s}\right)^2 \sigma_s^2}. \quad (4)$$

## 4 RESULTS

### 4.1 Earthquake catalogue

The derived earthquake catalogue has a total of 95 533 events from 1 June 2019 through 30 September 2019, with 94 839 of the events inside our focus region (Fig. 2), associated with  $\sim 2.5 \times 10^6$   $P$ -

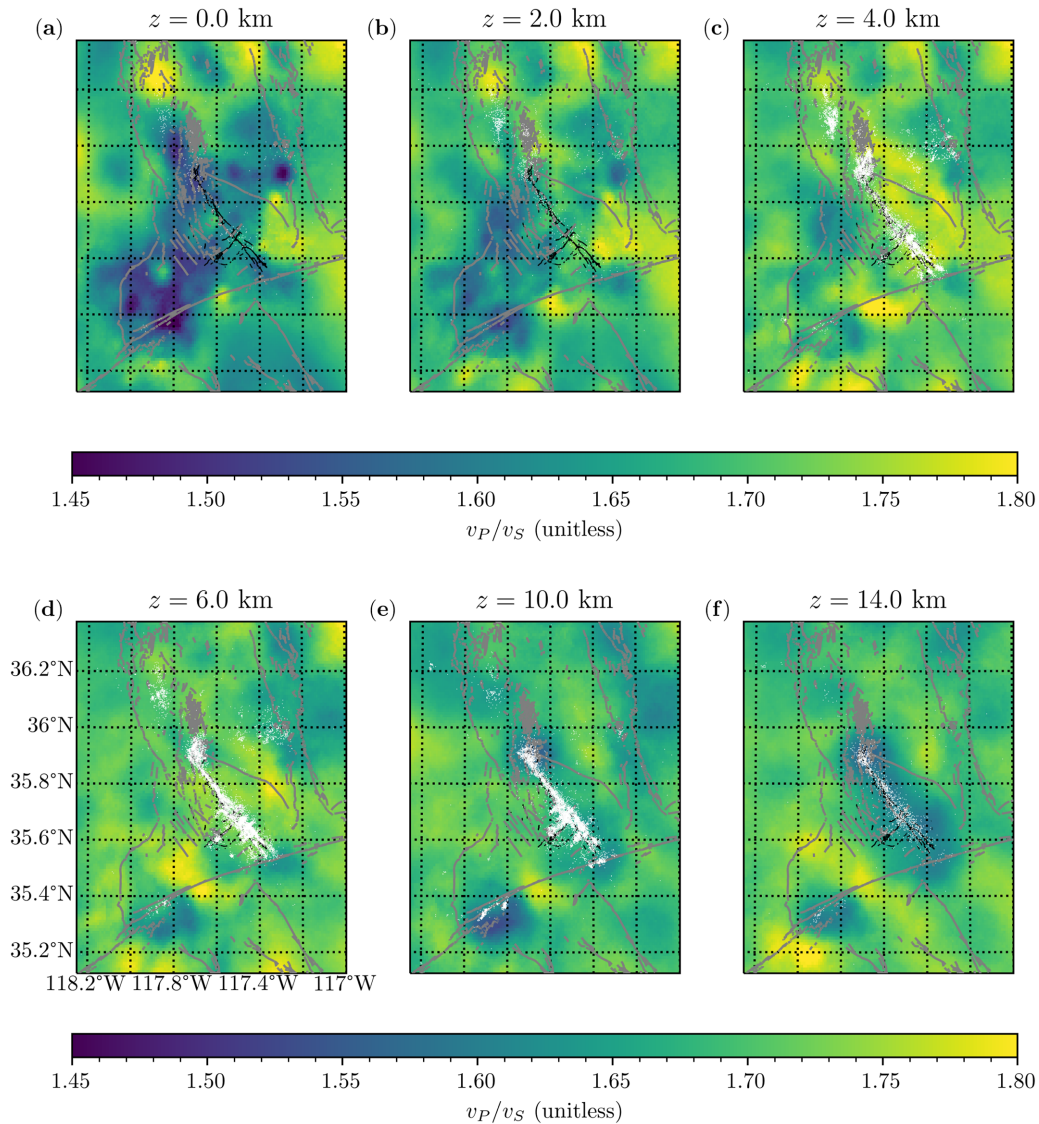


**Figure 10.** Horizontal slices through our  $V_p/V_s$  model, as discussed in Fig. 8.

and  $\sim 1.5 \times 10^6$   $S$ -wave arrival times. The catalogue is complete above  $M_L$  1.81 (Fig. 3) and exhibits sharp increases in the daily event detection rate at the times of the  $M_w$  6.4 and  $M_w$  7.1 main shocks, reflecting the increased seismicity rate of the aftershock sequences (Fig. 4). A second sharp increase in the daily detection rate coincides with the first phase of the dense deployment (3J.R) on 14 July 2019, followed by a gradual decrease corresponding to the decaying aftershock intensity. The second phase of the dense deployment (starting 8 August 2019) does not produce a corresponding increase in the daily event detection rate because many of the additional sensors were deployed in the 3J.G array on the Garlock Fault, which sustained relatively modest seismicity rates.

The detected seismicity can generally be categorized into five distinct groups associated with (i) the eastern Little Lake Fault (ELLF; Plesch *et al.* 2020), (ii) the southern Little Lake Fault (SLLF), (iii) the Fremont Valley, (iv) the Coso Range and (v) the Argus Mountains and Panamint Valley—although it is difficult to differentiate seismicity on the ELLF from that on the SLLF where the two faults intersect. We briefly describe prominent characteristics of the spatial distribution of seismicity in each of these groups in the remainder

of this section. Seismicity of the ELLF and beneath the Fremont Valley are discussed in greater detail in Section 4.3.

#### 4.1.1 Eastern Little Lake Fault

The majority of observed seismicity is associated with the ELLF. Seismicity in this group collapses to a relatively narrow volume ( $\sim 5$  km wide between 4 and 16 km deep) over a lateral interval of approximately 20 km, where the main rupture cuts through the Quaternary alluvium of the Indian Wells Valley (Figs 2 and 7). Events along this segment of the ELLF occur predominantly between 2 and 10 km depth and define a single simple lineation in map view. To the southeast of this localized segment, where the main fault intersects granodiorites of the Argus Mountains, seismicity diffuses through a complex network of southwest-/northeast-trending structures that intersect the ELLF at nearly right angles. Further to the southeast, seismicity gradually shallows towards the Garlock Fault and trifurcates into three discrete branches before abruptly deepening near the Garlock Fault. Whereas three distinct branches of seismicity characterize the southeast end of this main group of aftershocks,

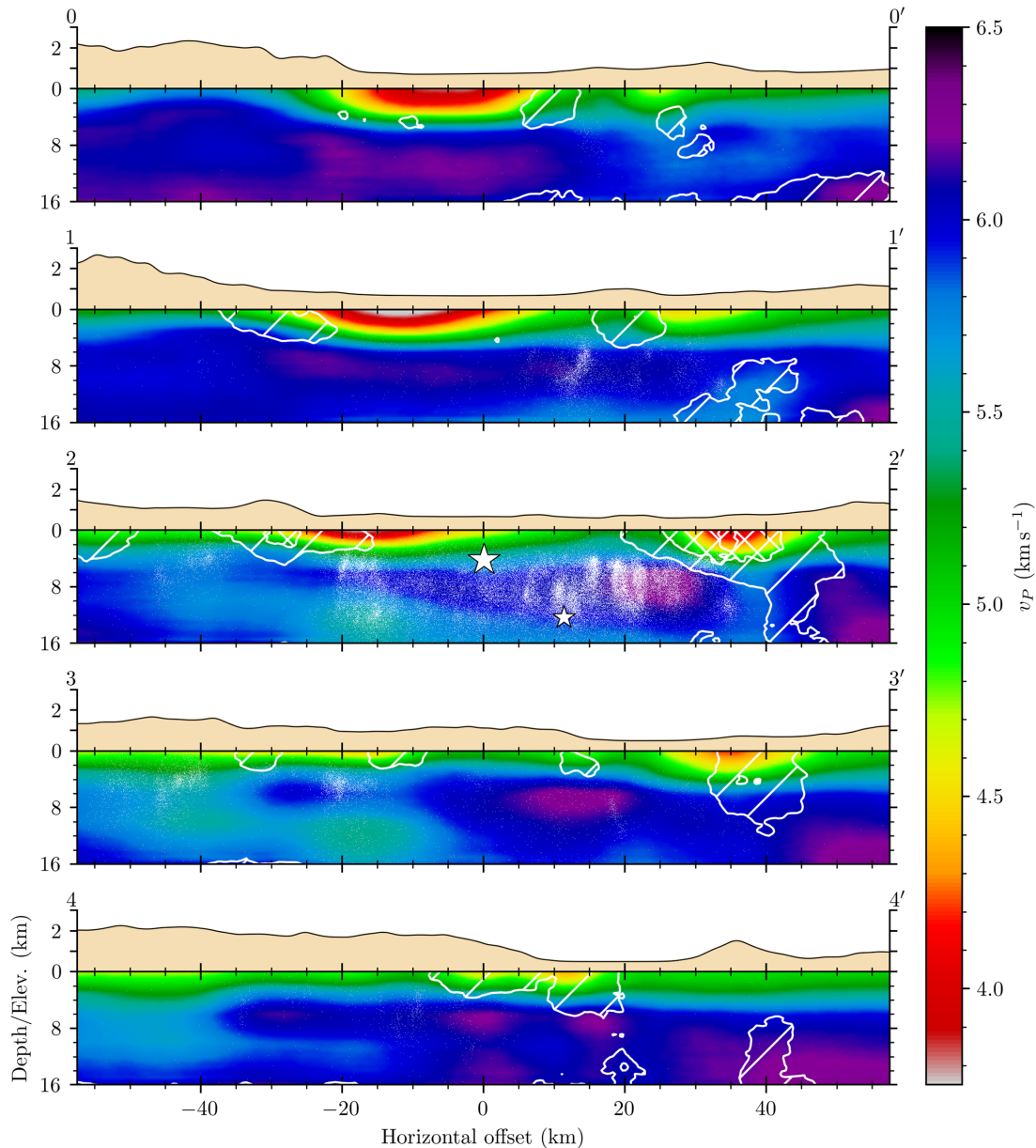


**Figure 11.** NW/SE trending, fault-parallel vertical slices (traces 0–0′ through 4–4′ on Fig. 2) of our  $V_p$  model at 10 km intervals. Seismicity within  $\pm 5$  km of each vertical plane is projected onto the plane and shown as white dots. The large and small stars on section 2–2′ mark the projected locations of the  $M_w$  7.1 and  $M_w$  6.4 main shocks, respectively. Solid white lines indicate contours of relative uncertainty,  $\sigma_P$ . The single- and cross-hatch patterns indicate regions where  $1.75$  per cent  $\leq \sigma_P < 2.5$  per cent and  $2.5$  per cent  $\leq \sigma_P < 5$  per cent, respectively and  $\sigma_P < 1.75$  per cent in unhatched regions.

seismicity at the northwest end, near the foot of the Coso Range, diffuses through a portion of the crust subtended by the ELLF and an  $\sim 10$ -km-long, orthogonally oriented feature that delineates the northwest terminus of the aftershocks associated with the ELLF.

#### 4.1.2 Southern Little Lake Fault

Much of the seismicity associated with the SLLF is difficult to differentiate from that associated with the ELLF because the two intersect, and we observe the most diffuse spatial distribution of seismicity around the intersection. One distinct cluster of seismicity, however, occurs near the southwest end of the SLLF between 4 and 8 km depth. Events associated with the SLLF span  $\sim 20$  km along the fault and are flanked on the northwest and southeast by multiple

parallel lineations that crosscut the ELLF (the complex network of intersecting features referred to in the paragraph above) and give insight into stepover kinematics.

#### 4.1.3 The Garlock Fault and Fremont Valley

In addition to the deep seismicity at the southeast end of the  $M_w$  7.1 rupture, the Garlock Fault hosts an isolated swarm of deep seismicity ( $\sim 8$  to 12 km deep) beneath the Fremont Valley to the southwest of the main rupture. This area was targeted by the second phase of the dense deployment (i.e. the 3J.G subarray). The Fremont Valley occupies the region between two strands of the Garlock Fault that are separated by a stepover, and this swarm of deep seismicity occurred entirely within this stepover region, primarily along two

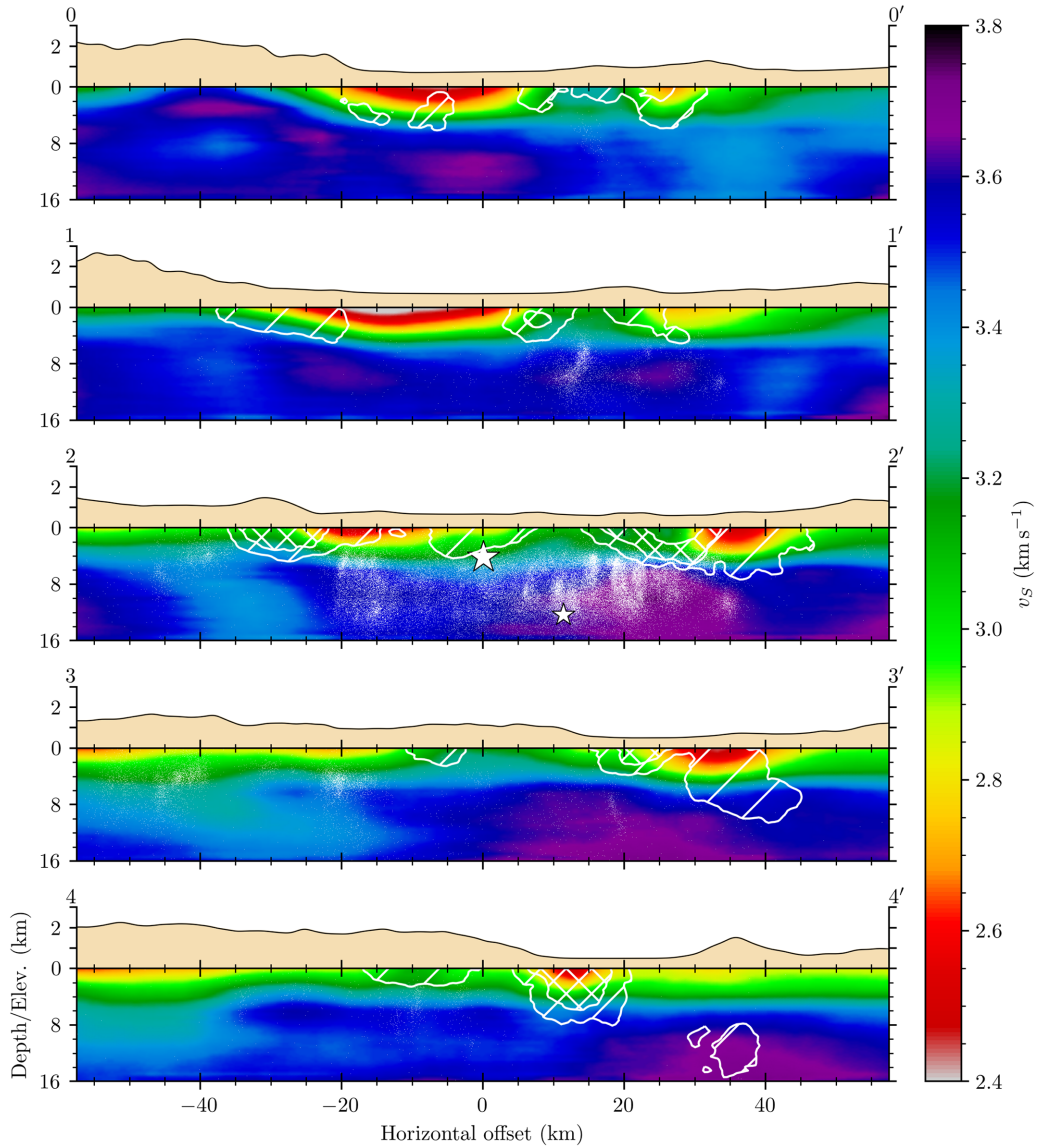


**Figure 12.** Vertical slices through our  $V_s$  model, as discussed in Fig. 11. As in Fig. 11, the single- and cross-hatch patterns indicate regions where 1.75 per cent  $\leq \sigma_S < 2.5$  per cent and 2.5 per cent  $\leq \sigma_S < 5$  per cent, respectively and  $\sigma_S < 1.75$  per cent in unhatched regions.

northeast-/southwest-trending lineations that apparently dip to the southeast. Although the number of events here is relatively small ( $\sim 2500$ ), these events are valuable because they illuminate structure on the enigmatic Garlock Fault that would otherwise remain obscure.

#### 4.1.4 Coso Range

A conspicuous seismic gap characterizes the Coso Range south of the Coso Volcanic Field, and to the northwest of this seismic gap, there lies a roughly 20 by 10 km patch of shallow ( $< 6$  km deep) seismicity. Activity in this region was contemporaneous with that in the main rupture area and forms three substructures: (i) a very shallow fan of seismicity at the southern end; (ii) four pockets of seismicity at the north end of the shallow fan and (iii) a linearly distributed cluster north of the four pockets of seismicity.

#### 4.1.5 Argus Mountains

A final group of earthquakes forms isolated pockets distributed over a broad region approximately parallel to the Garlock Fault in the Argus Mountains and further east, starting roughly 15 km to the east of the diffuse seismicity at the northwest end of the ELLF. The distinct clusters of shallow events that compose this area of seismicity exhibit a weak east/west trend and seem to occur preferentially in regions where the surface geology is igneous (Fig. 7), such as in the Argus Mountains, in contradistinction to regions where the surface geology is sedimentary, such as in the Searles and Panamint valleys.

## 4.2 Velocity models

We derive 3-D models of  $V_p$ ,  $V_s$  and  $V_p/V_s$  structure using the entire earthquake catalogue described above and four different starting models (CVMH, CVMS, HK1D and FANG3D). In this section, we focus on our preferred model, which was derived from the CVMH starting model; additional results are available

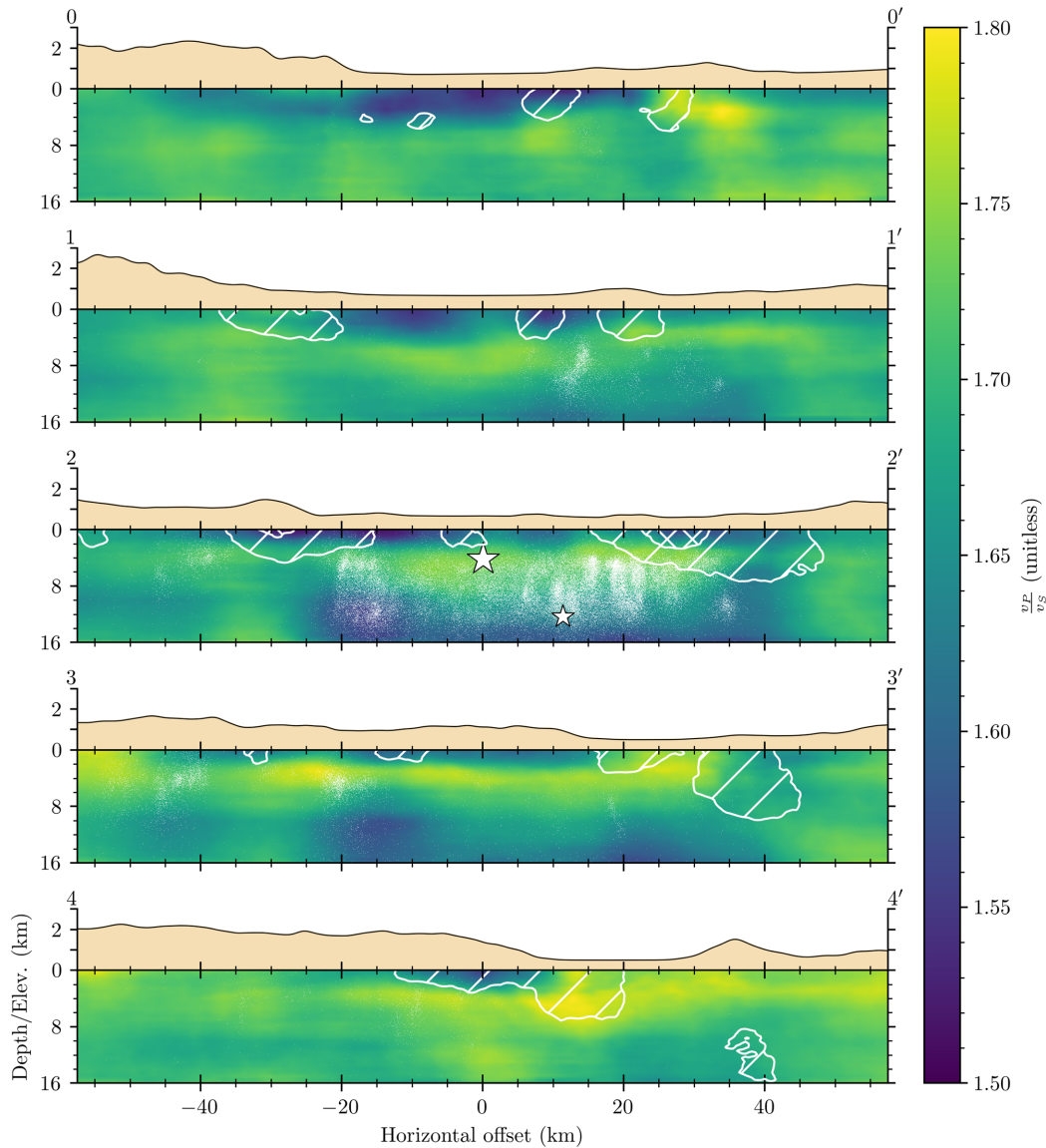


**Figure 13.** Vertical slices through our  $V_p/V_s$  model, as discussed in Fig. 11. The single- and cross-hatch patterns indicate regions where 2.5 per cent  $\leq \sigma_{P/S} < 5$  per cent and 5 per cent  $\leq \sigma_{P/S} < 10$  per cent, respectively and  $\sigma_{P/S} < 2.5$  per cent in unhatched regions.

in the Supplementary Material. The derived models correlate well with surface geology and observed spatial seismicity patterns. In the following, we describe model residuals (Fig. 5), resolution (Fig. 6), robustness and salient model features in relation to surface geology and spatial seismicity patterns. In Section 5, we discuss our interpretations of the models.

#### 4.2.1 Model residuals, resolution and robustness

Each of the starting models produces a final model with comparable distributions of residuals between observations and model predictions (Fig. 5), with the 1-D starting model yielding the largest misfit. Although our preferred model has larger residuals for  $S$ -wave data than the other two 3-D starting models, we prefer it for its smoothness, consistency with surface geology, and its relatively modest uncertainty (particularly in comparison with the CVMS starting model). The standard deviation of residuals was reduced from 0.334 s (with 0.081 s mean) in the initial model to 0.295 s

(with 0.007 s mean) in the preferred model for  $P$  waves and from 0.479 s (with  $-0.127$  s mean) to 0.387 s (with  $-0.014$  s mean) for  $S$  waves.

To assess model resolution, we perform a series of checkerboard tests, in which  $\pm 5$  per cent anomalies are superimposed on a 1-D background model and synthetic arrival times without added noise are used. We present an illustrative example here (Fig. 6); additional results are available to the interested reader in the Supporting Information.

The recovered checkerboard models indicate that, as expected, model resolution is best within the footprint of the dense deployment and degrades progressively outside of it. The recovered models resolve internal detail of fine-scale anomalies ( $\sim 10$  km horizontal and  $\sim 4$  km vertical extent) as deep as 16 km in key areas of the focus region; however, the top 3 km of the crust (i.e. 2 km below sea level) are poorly resolved throughout the model, as are regions deeper than 16 km. The relative northeast/southwest displacement between seismicity on the main faults (ELLF, SLLF and Garlock) and the

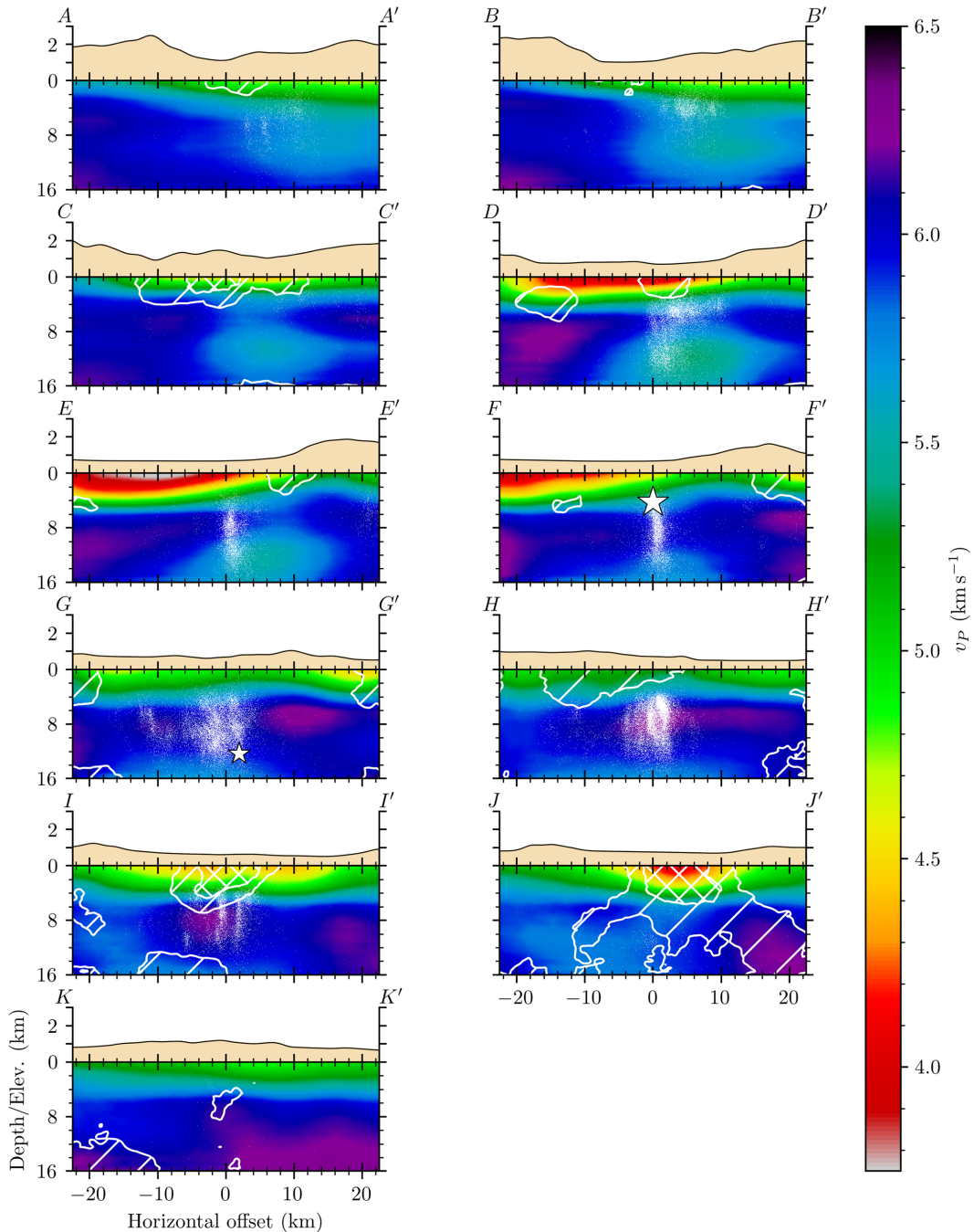


**Figure 14.** SW/NE trending fault-normal vertical slices (traces  $A - A'$  through  $K - K'$  on Fig. 2) through our  $V_p$  model, as discussed in Figs 11–12. Relative-uncertainty contours are as in Fig. 11.

dense deployment arrays (3J.R and 3J.G) imparts an overall north-east/southwest trend to the region of the model that is well resolved.

Major model features interpreted below are generally consistent for different starting models where checkerboard tests indicate good resolution, with the exception of the low-velocity zone (LVZ) below 6 km depth associated with the Coso Volcanic Field (discussed below), which is absent in the models derived from the HK1D and, to a lesser extent, the FANG3D model. This model feature is, however, believed to be realistic because an associated LVZ to the SE below 8 km depth exists in all derived models and the oversimplified velocity structure in the model derived from the HK1D starting model is difficult to interpret in light of the heterogeneity we expect

the Coso Volcanic Field to introduce. Thus, although the geometrical details and amplitudes of anomalies depend on the starting model, their first-order characteristics are robust and justify modest interpretation.

#### 4.2.2 Surface geology and shallow velocities

Correlating our velocity models with surface geology provides a first-order method of validating our models of the shallow crust, and we indeed find strong correlations with our  $V_p$ ,  $V_s$  and  $V_p/V_s$  models (Fig. 7). Large-scale features can be generally described as

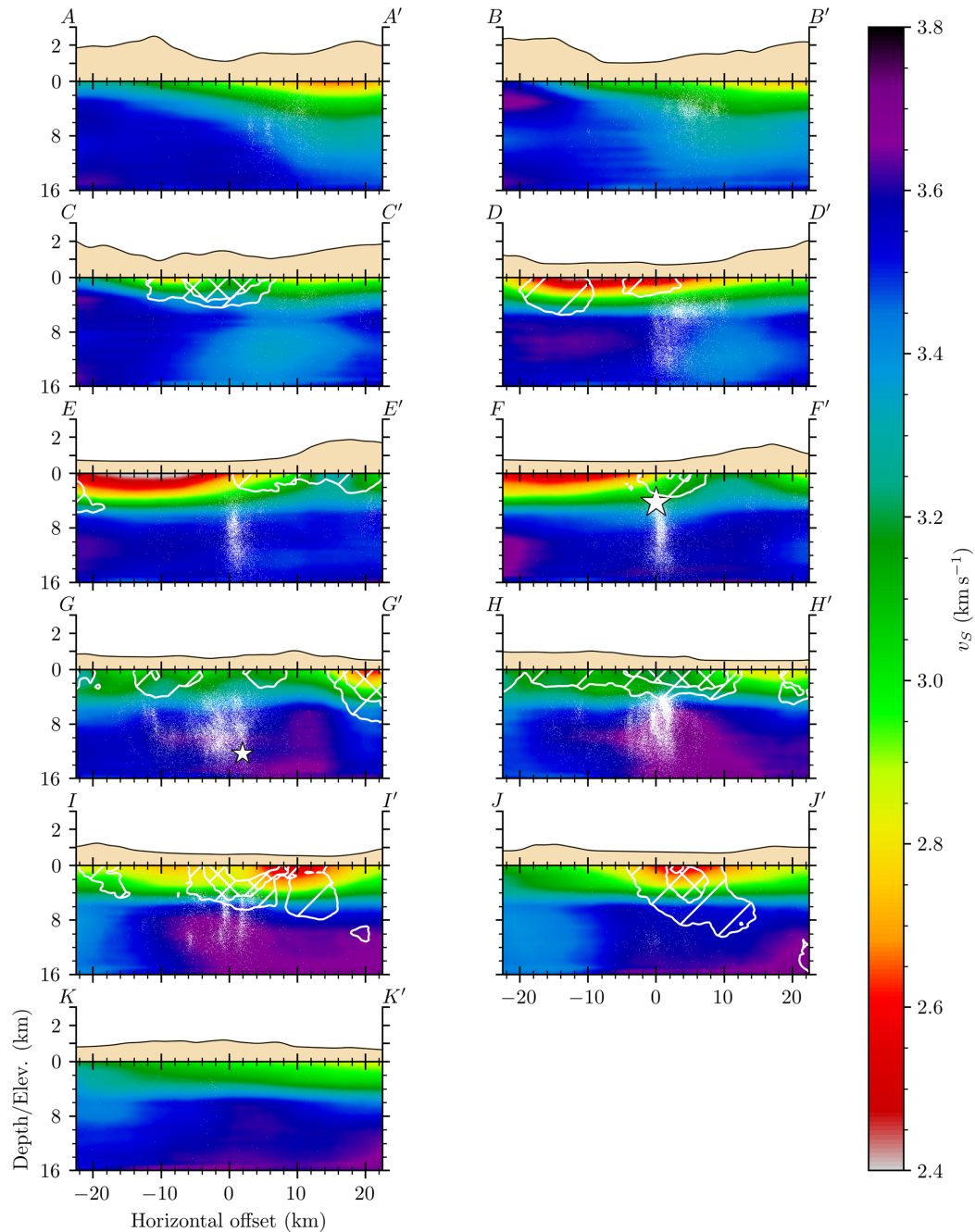


**Figure 15.** SW/NE trending fault-normal vertical slices through our  $V_s$  model, as discussed in Fig. 14. Relative-uncertainty contours are as in Fig. 12.

(i) high-velocity regions with  $V_p/V_s > 1.70$  coinciding with the predominantly igneous composition of the southeastern Sierra Nevada, Coso, Argus, El Paso and Rand mountains and (ii) low-velocity regions with  $V_p/V_s < 1.70$  coinciding with alluvium in the Indian Wells, Panamint, Fremont and Searles valleys.

The highest  $V_p$  and  $V_s$  values in the shallow crust are found in the Sierra Nevada Mountains; however, station coverage is poor in this region, and our inversion cannot constrain much of this structure beyond the initial model, resulting in high-velocity ‘bullseye’ features. Comparable  $V_p$  values characterize the Coso, Argus, El Paso, and Rand mountains, but values in the Coso and Argus mountains are notably lower than those in the Sierra Nevada Mountains—possibly because the lithology associated with the Sierra Nevada

Mountains extends to greater depths, making the structure easier to resolve. Alluvium overlies granodiorite at the intersection between the ELLF and the Argus Mountains, which manifests as a region of locally reduced  $V_p$  relative to the higher  $V_p$  associated with exposed granodiorite north and south of the intersection. These low  $V_p$  values may also be related to rock damage associated with the SLLF and ELLF (Qiu *et al.* 2020).

The lowest  $V_p$  and  $V_s$  values in the shallow crust are found in the Indian Wells Valley, and the associated basin structure in our models coincides with the shape of the basin, as inferred from the surface geology. Our models show a steep velocity gradient at the edge of the basin at the foot of the Sierra Nevada Mountains but a more gradual transition zone at the Coso and Argus mountains.

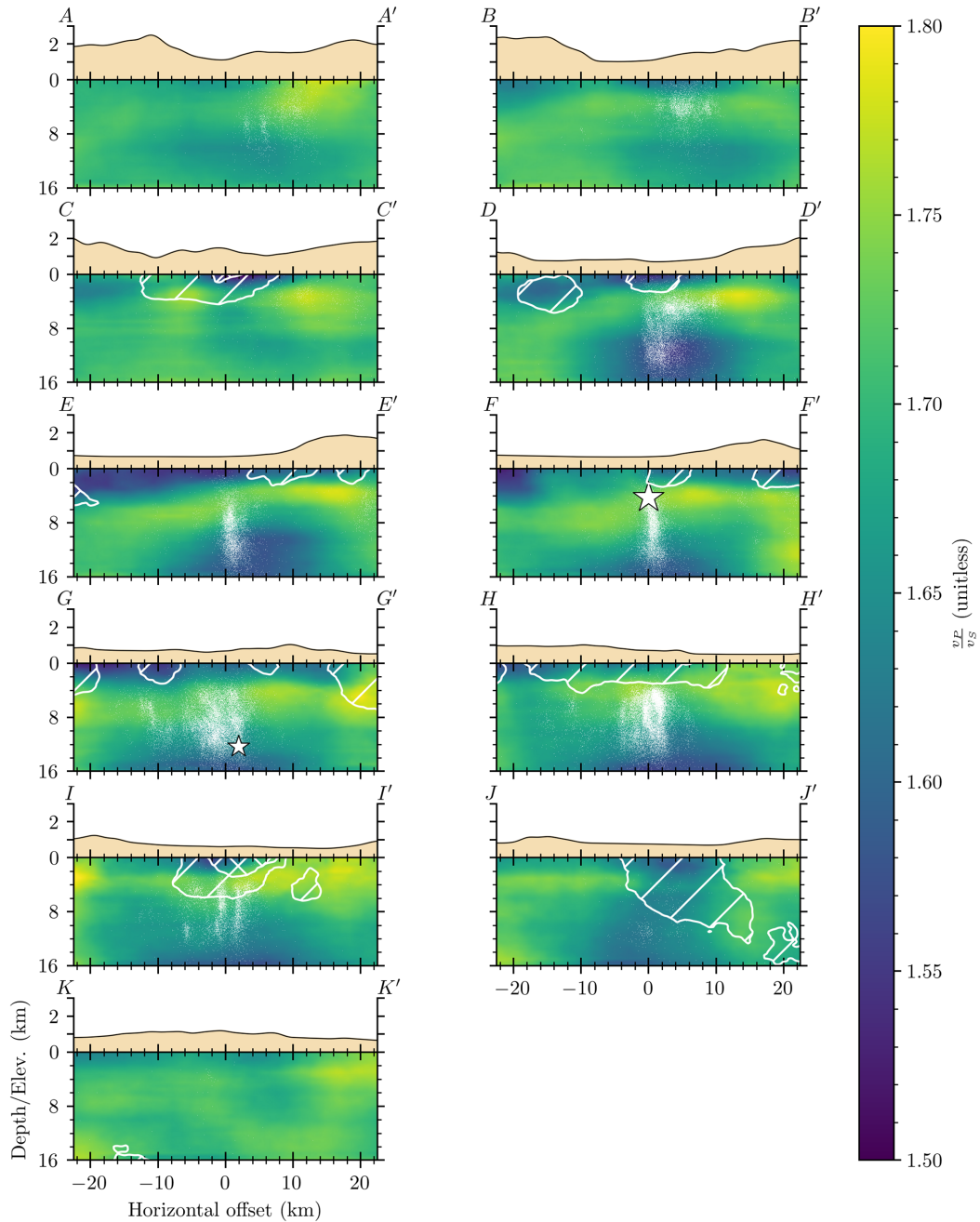


**Figure 16.** SW/NE trending fault-normal vertical slices through our  $V_p/V_s$  model, as discussed in Fig. 14. Relative-uncertainty contours are as in Fig. 13.

The Garlock Fault cuts through two low-velocity regions. The first, at the SE end of the ELLF, correlates with sedimentary geology of the Searles Valley and may have played a key role in terminating the  $M_w$  7.1 rupture. The second coincides with the fault stepover in the Fremont Valley and the associated swarm of deep seismicity there. Both of the features also coincide with reduced  $V_p/V_s$ , and they are separated by a region of high  $V_p/V_s$  that correlates well with rhyolitic surface geology. We discuss these features in greater detail in Section 5.

#### 4.2.3 Horizontal slices

Our velocity models generally decorrelate with surface geology below 4 km depth (Figs 8–10). Prominent  $V_p$  and  $V_s$  low-velocity

zones (LVZs) are observed near the northwest end of the ELLF below 6 km depth; however, they do not coincide exactly. The  $V_p$  LVZ is only faintly visible at 6 km depth, is most prominent at 10 km depth, and migrates toward the southeast with increasing depth, localizing directly beneath the northwest terminus of the ELLF. The  $V_s$  LVZ, on the other hand, is most prominent near 6 km depth and shows little lateral migration with depth, suggesting laterally varying fluid content. A region of low  $V_p/V_s$  occurs at 10 km depth, where the  $V_p$  LVZ localizes beneath the northwest terminus of the ELLF and grows to envelope the entire ELLF by 14 km depth. A similar  $V_p/V_s$  feature is observed as shallow as 6 km deep beneath the Fremont Valley. This low  $V_p/V_s$  feature beneath the Fremont Valley is the result of a colocated  $V_p$  LVZ without a corresponding  $V_s$  LVZ. In this instance, the low  $V_p/V_s$  feature is most

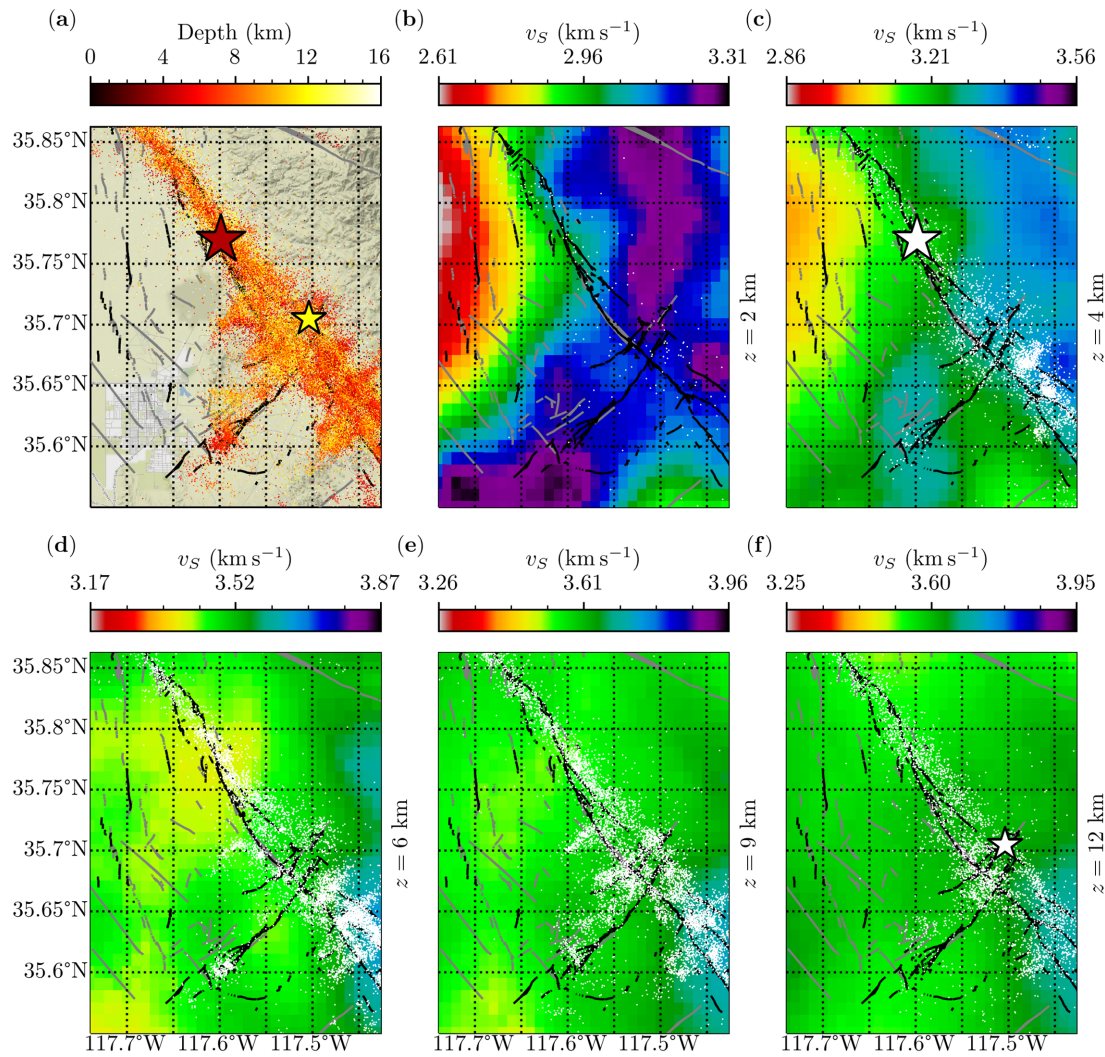


**Figure 17.** (a) Seismicity in the region surrounding the central segment of the ELLF and (b)–(f) horizontal slices of the  $V_s$  model at 2, 4, 6, 9 and 12 km depth.

prominent at 10 km depth. This leads us to an important observation of this study: deep earthquake source regions associated with the Ridgecrest earthquake correlate with regions of low  $V_p$  and  $V_p/V_s$ . To the east of the Fremont Valley, a  $V_s$  LVZ below 6 km depth with high  $V_p/V_s$  between 0 and 14 km depth coincides with rhyolitic surface geology and a segment of the Garlock Fault, along which Barnhart *et al.* (2019) observed aseismic surface creep.

#### 4.2.4 Structural variability parallel to the ELLF

Vertical cross sections taken parallel to the ELLF (0–0' through 4–4'; Figs 2 and 11–13) elucidate variable seismicity patterns and velocity structure along the strike of the ELLF and with depth.

The majority of observed seismicity ( $\sim 77$  per cent) occurred within 5 km of the primary trace of the ELLF (section 2–2'), and the  $M_w$  7.1 main shock occurred in a region with a fault-parallel gradient in  $V_s$  below 6 km depth (Fig. 12). Southeast of the main shock, where most aftershocks occurred, our  $V_s$  model has stable values near  $\sim 3.7$   $\text{km s}^{-1}$ , consistent with  $V_s$  expected of granitic to dioritic composition in that depth range (Christensen 1996). Our  $V_p$  model shows a maximum value of  $\sim 6.3$   $\text{km s}^{-1}$  in the same region, consistent with velocities expected for the granitic–diorite range of composition, although the spatial extent of

this feature in our  $V_p$  model differs from that in the  $V_s$  model, which produces a correspondingly low  $V_p/V_s$  region and may be evidence of faulting, fracturing, or temperature differences. To the northwest of the main shock,  $V_s$  decreases to  $\sim 3.55$   $\text{km s}^{-1}$  and  $V_p$  is limited to  $\sim 6.0$   $\text{km s}^{-1}$  in a wedge-shaped structure that pinches out to the northwest;  $V_p$  beneath the wedge is as low as  $\sim 5.5$   $\text{km s}^{-1}$ .  $V_p$  within the wedge is consistent with that of a granitic gneiss, and decreased  $V_p$  below the wedge can be explained by increased temperature or shearing. Average  $V_p$  and  $V_s$  values between 4 and 12 km depth beneath the Coso Volcanic Field (near  $-40$  km horizontal offset in Figs 11 and 12) of  $\sim 5.8$  and  $3.5$   $\text{km s}^{-1}$ , respectively, are consistent with various lithologies including basaltic, which is a favourable interpretation because it is consistent with nearby surface geology.

#### 4.2.5 Fault-normal sections

Vertical cross sections taken perpendicular to the ELLF ( $A - A'$  through  $K - K'$ ; Figs 2 and 14–16) elucidate variable seismicity patterns and velocity structures across the ELLF and with depth.

A lateral gradient from the higher velocity crust beneath the Sierra Nevada Mountains to the lower velocity crust beneath the Coso Range characterizes the northwesternmost fault-normal profiles (sections  $A - A'$  and  $B - B'$ ). The velocity gradient in the

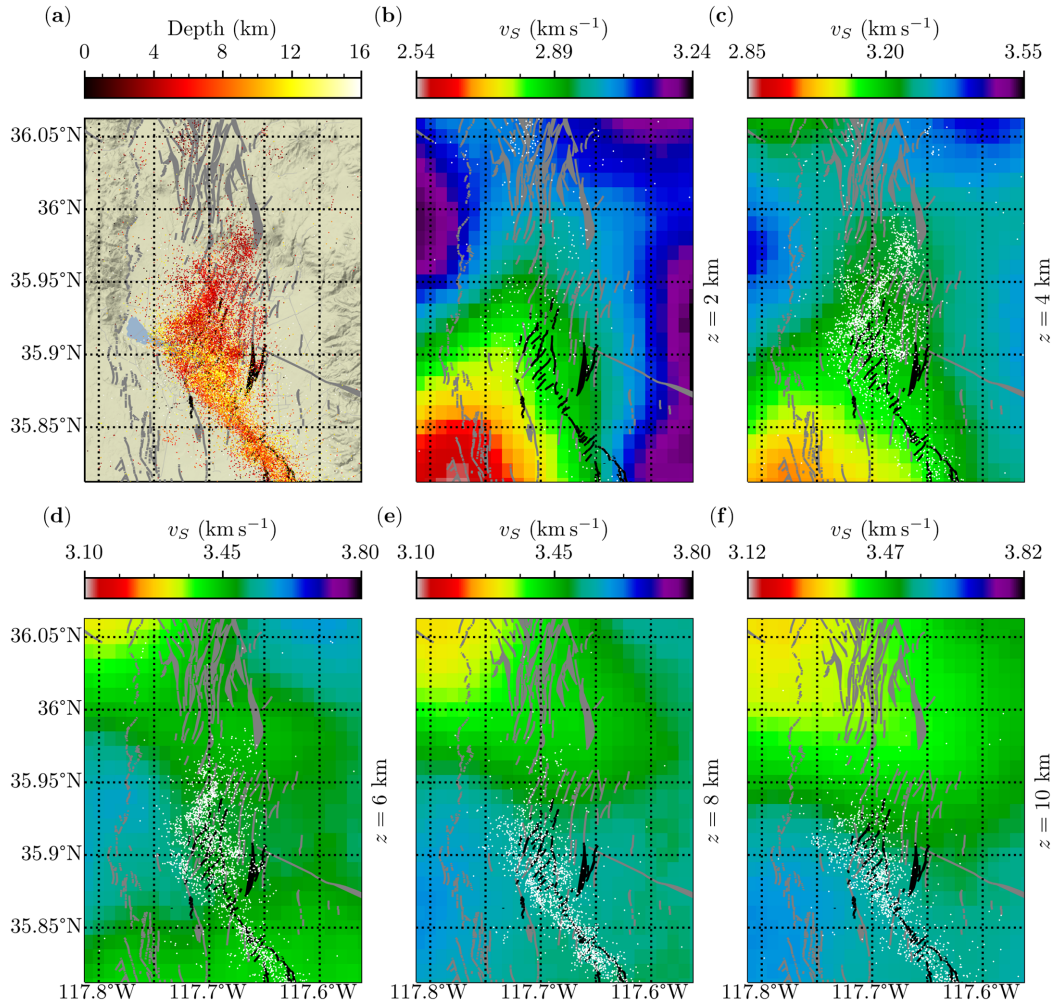


**Figure 18.** (a) Seismicity in the region surrounding the northwest terminus of the ELLF and (b)–(f) horizontal slices of the  $V_s$  model at 2, 4, 6, 8 and 10 km depth.

top 4 km of the crust reverses (low on the southwest and high on the northeast) near the Coso Volcanic Field (section  $C - C'$ ), with velocities below 4 km depth gradually transitioning to a more homogeneous distribution in sections  $D - D'$  through  $F - F'$ . Strong lateral velocity gradients in the top 4 km decrease in sections  $G - G'$  through  $K - K'$ , except for low-velocity basins in sections  $I - I'$  and  $J - J'$ , and the cross-fault velocity contrast reverses polarity southeast of section  $F - F'$  (along which the projected hypocentre of the  $M_w$  7.1 event occurred), with the northeast side of the fault being higher velocity than the southwest side.

Seismicity patterns are simplest where lateral velocity structure is relatively homogeneous (e.g. sections  $E - E'$  and  $F - F'$ ), whereas seismicity is more complex and broadly distributed where lateral velocity gradients exist (e.g. sections  $D - D'$  and  $G - G'$  through  $I - I'$ ).

### 4.3 Key structural features

#### 4.3.1 Central ELLF

The  $M_w$  6.4 earthquake nucleated in a region with a strong  $V_s$  gradient across the SLLF at 12 km depth and propagated primarily to the southwest towards a LVZ (Fig. 17). Similarly, the  $M_w$  7.1

earthquake nucleated in a region with strong  $V_s$  gradients along and across the ELLF at 4 km depth. The entire central segment of the ELLF is characterized by cross-fault  $V_s$  contrasts (slower on the southwest) in the top 4 km, with the steepest gradients to the northwest of the  $M_w$  7.1 and southeast of the  $M_w$  6.4 at 4 km depth.

#### 4.3.2 Northwest ELLF

At the northwest terminus of the ELLF, a cross-fault  $V_s$  contrast is observed below 6 km depth, with the low-velocity side to the northeast (Fig. 18). Above 6 km depth, this  $V_s$  contrast reverses. Similarly, relatively low  $V_s$  to the north of the fault terminus (below 6 km depth) is replaced by relatively high velocities above 6 km.

#### 4.3.3 Southeast ELLF

The southeast terminus of the ELLF exhibits a strong fault-parallel  $V_s$  gradient that decreases toward the southeast in the shallow crust (top 4 km), where seismicity trifurcates and shallows (Fig. 19). Below 6 km depth, high  $V_s$  localizes to a ‘bullseye’ that encloses the trifurcation region.

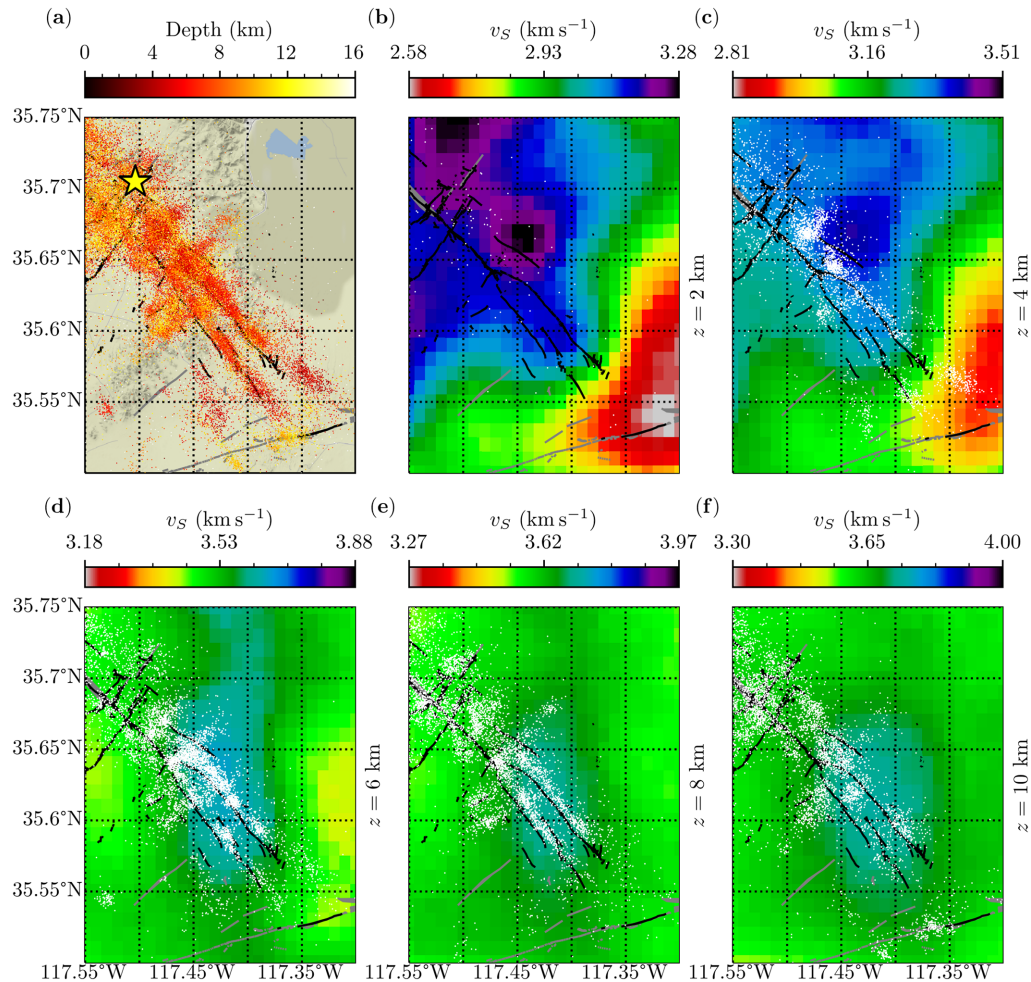


**Figure 19.** (a) Seismicity in the region surrounding the southeast terminus of the ELLF and (b)–(f) horizontal slices of the  $V_s$  model at 2, 4, 6, 8 and 10 km depth.

#### 4.3.4 Garlock Fault at Fremont Valley

The low  $V_s$  of sediment in the Fremont Valley is clearly apparent in the shallow crust (top 4 km; Fig. 20). Moderately reduced  $V_s$  is also observed at 8–10 km depth in a region that is bound on the north and south by mapped strands of the Garlock Fault and to the east and west by detected seismicity. Bounding seismicity to the east and west form roughly northeast-/southwest-trending lineations that apparently dip to the southeast.

## 5 DISCUSSION AND CONCLUSIONS

We processed 4 months of raw waveform data recorded starting 1 month before the  $M_w$  6.4 and  $M_w$  7.1 main shocks using automated procedures to derive an earthquake catalogue with over 95 000 events. We then perform 3-D, ray-based tomography modeling using data from this catalogue to relocate earthquakes and obtain detailed models of seismic  $P$ - and  $S$ -wave speeds ( $V_p$  and  $V_s$ ) and their ratio  $V_p/V_s$ . Our derived seismic catalogue contributes to the growing list of earthquake catalogues for the 2019 Ridgecrest earthquake sequence (Lee *et al.* 2020a,b; Lin 2020; Liu *et al.* 2020; Lomax 2020; Ross *et al.* 2019; Shelly 2020), but our catalogue is unique in at least three ways: (i) it is the only catalogue derived using recordings from the rapid-response dense-deployment of seismometers (Catchings *et al.* 2020); (ii) it is the temporally

longest catalogue, focusing exclusively on the Ridgecrest event sequence and (iii) it is the only catalogue built using fully 3-D location methods and velocity model updates. Our catalogue contributes the largest number of new phase arrival times to the standard catalogue from the SCSN. Furthermore, the events in our catalogue can be used as templates to detect many more events that produce similar waveforms (e.g. Shelly *et al.* 2016; Ross *et al.* 2017).

The velocity structure in the upper 8 km of the crust along the segment of the ELLF southeast of the  $M_w$  7.1 epicentre is characterized by relatively high  $V_p$  and  $V_s$  beneath the Argus Mountains and Spangler Hills and low  $V_p$  and  $V_s$  near the southeastern end of the rupture, where it abuts the Garlock Fault. The network of orthogonal branches of seismicity along this segment of the  $M_w$  7.1 fault have been noted in other studies (e.g. Ross *et al.* 2019) and are reminiscent of the ‘shatter networks’ observed near the Trifurcation Area of the San Jacinto Fault Zone (White *et al.* 2019). These complex structures may result from failure of highly brittle crust, a hypothesis consistent with high shear moduli that explains the observed elevated  $V_p$  and  $V_s$ . Strain diffuses across three sub-parallel strands of seismicity, where the highest seismic velocities along the ELLF are observed (immediately northwest of the Garlock Fault). The abrupt deepening of seismicity near the Garlock Fault may result from a highly compliant (i.e. low shear moduli and thus low-velocity) crust associated with the Garlock Fault that

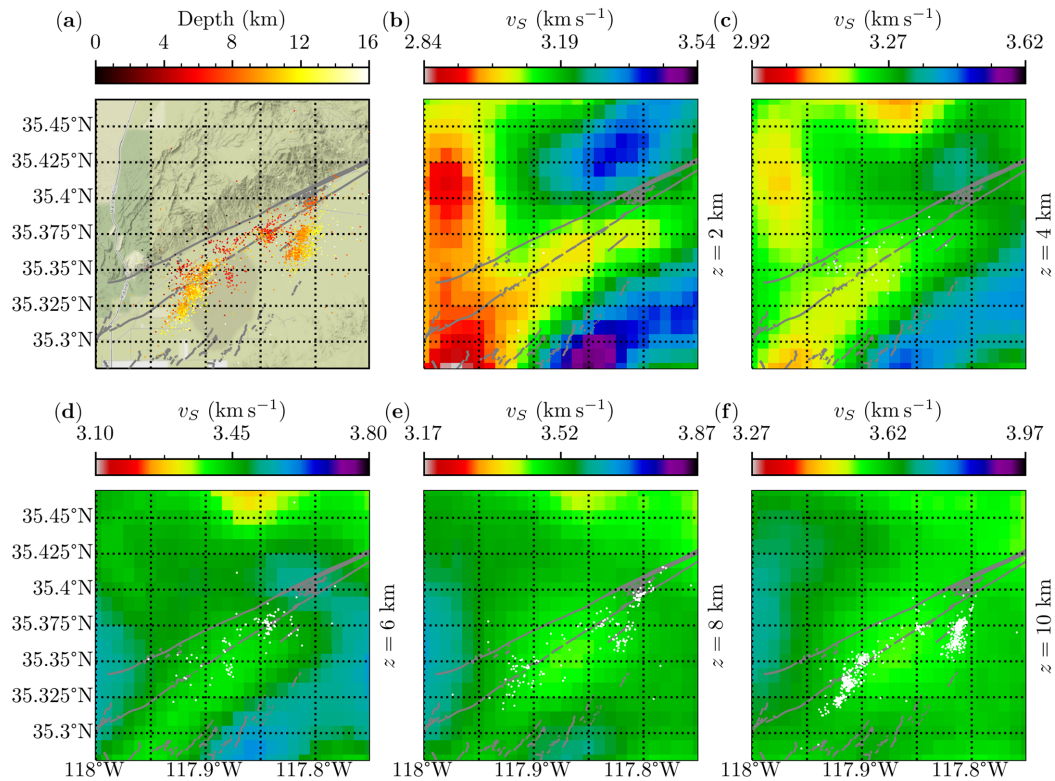


**Figure 20.** (a) Seismicity in the region of the Fremont Valley and (b)–(f) horizontal slices of the  $V_s$  model at 2, 4, 6, 8 and 10 km depth.

absorbs strain and reduces the stress at shallow depths below the level needed to produce brittle failure of detectable magnitude. This highly compliant portion of the crust, which we interpret as due to a combination of weak sedimentary lithology at the surface and fault damage at depth, likely played a key role in terminating the southeast rupture of the ELLF during the  $M_w$  7.1 main shock by readily deforming and dissipating the stress.

Northwest of the  $M_w$  7.1 epicentre, the ELLF penetrates the Indian Wells Valley, and aftershock activity localizes along a single linear (in map view) zone. Cross-fault velocity contrasts as large as 10.5 per cent for  $V_p$  and 13.8 per cent for  $V_s$  in the upper 4 km of crust along this segment of the ELLF suggest that a bimaterial interface at the edge of the Indian Wells Valley may have played a key role in localizing the rupture along this fault segment (e.g. Brietzke & Ben-Zion 2006). Seismicity at the northwest end of the ELLF terminates along a zone that trends orthogonal to the ELLF, near the transition between Indian Wells Valley and the Coso Mountains. Apparently, the rupture on the ELLF did not have sufficiently concentrated stress to penetrate the more rigid (higher velocity) Coso Mountains and was diverted to failures in the weaker (slower) sediments of the Indian Wells Valley. The high angle between ruptures in the Indian Wells Valley and the Ridgecrest area is expected of ruptures that decelerate rapidly upon encountering a barrier (Xu & Ben-Zion 2013). We hypothesize that opposing structures caused the arrest of the  $M_w$  7.1 rupture of the ELLF at either end: (a) a strong barrier to the northwest (i.e. the Coso Mountains) that the rupture could not penetrate, and (b) a compliant buffer that dissipated stress to the southeast (i.e. the Garlock Fault).

The proposed hypothesis, which is necessarily retrospective, is primarily intended to be explanatory, not predictive. Our aim is not to suggest a predictive framework for earthquake cessation, but rather to propose potential mechanisms that explain the cessation of

this single earthquake. Only after many similar observations would we hope to extract patterns with predictive power. We suggest then, that the hypothesis be used not to make predictions about where a future earthquake rupture might arrest, but to guide future research looking for earthquake cessation patterns that may eventually yield such predictive capacity.

It is interesting to note that where seismicity trifurcates at the southeastern end of the ELLF, it penetrates a region with greater  $V_s$  (and thus greater rigidity) than the region that we hypothesize acted as a rigid barrier at the northwestern end. This indicates that our hypothesis is, at best, an incomplete explanation. The variables that affect the ability of a rupture front to penetrate a rigid body are manifold: for example the amount of stress concentrated along the rupture front, the rupture orientation with respect to the boundary of the rigid body and any internal planes of weakness, the geometry of the rigid body, and the geometry of the rupture front. Speculating on the effect of these variables in the present case is beyond the scope of this paper, as they are either unknown or uncertain, but their effects might be systematically tested in a laboratory or computational environment.

The isolated swarm of seismicity in the stepover region along the Garlock Fault form northeast-/southwest-trending lineations that extend between the two main branches of the Garlock Fault. Given the right-lateral sense of motion on the ELLF during the main rupture, these lineations likely represent accommodation of transtensional stresses induced on the Garlock Fault by the  $M_w$  7.1 main shock in a pull-apart basin structure.

Our earthquake tomography model has low resolution in the shallow crust, where important velocities are needed for ground motion estimation (Seyhan & Stewart 2014; Juarez & Ben-Zion 2020), and our results are also unable to resolve internal fault detail in the immediate vicinity of the Ridgecrest rupture. Improved results

for the shallow crust can be obtained using active sources (e.g. Louie 2001; Schuster 2009) or the ambient seismic noise (e.g. Lin *et al.* 2013; Zigone *et al.* 2019). Detailed imaging of the rupture zone, on the other hand, is best accomplished using seismic phases that propagate along and across the fault zone and has been targeted in a separate study (Qiu *et al.* 2020). The velocity structure in our study area has various low-velocity zones at depth that are likely produced by a combination of lithological variations, fluids, temperature, and rock damage. Low  $V_p/V_s$  in deep earthquake source regions are consistent with the observations of Lin & Shearer (2009), which they interpreted as due to the presence of fluids (i.e. water). Using the derived catalogue to estimate earthquake-induced rock damage (Ben-Zion & Zaliapin 2019) can improve estimates of rock types and fluid content in various locations.

## ACKNOWLEDGMENTS

IRIS Data Services are funded through the Seismological Facilities for the Advancement of Geoscience (SAGE) Award of the National Science Foundation under Cooperative Service Agreement EAR-1851048. Research for this paper was supported by the National Science Foundation (grants EAR-1945781 and EAR-1722561) and the Southern California Earthquake Center (based on NSF Cooperative Agreement EAR-1600087 and USGS Cooperative Agreement G17AC00047). We thank Frederik Tilmann, Walter Mooney, an anonymous referee and Editor Ana Ferreira for useful comments that helped us to improve the manuscript.

## DATA AVAILABILITY

The derived seismic catalogue and  $V_p$ ,  $V_s$  and  $V_p/V_s$  velocity models can be obtained at <https://data.mendeley.com/datasets/x8v5wkbj6r> and <https://data.mendeley.com/datasets/gv33tgv5f>, respectively. All figures were created using Matplotlib (Hunter 2007). Numerous open-source Python packages were critical in completing this work, including but not limited to NumPy (Harris *et al.* 2020), SciPy (Virtanen *et al.* 2020), Pandas (McKinney 2010), ObsPy (Beyreuther *et al.* 2010) and IPython/Jupyter (Perez & Granger 2007). Focal mechanism data for the  $M_w$  6.4 and  $M_w$  7.1 main shocks shown in Fig. 1 were obtained from the USGS website at <https://earthquake.usgs.gov/earthquakes/eventpage/ci38443183/moment-tensor> (last accessed 14 December 2020) and <https://earthquake.usgs.gov/earthquakes/eventpage/ci38457511/moment-tensor> (last accessed 14 December 2020), respectively. The geological data shown in Fig. 7 were downloaded from the USGS website (<https://mrdata.usgs.gov/geology/state/state.php?state=CA>; last accessed 1 July 2020). Fault traces of Quaternary faults in Figs 1, 2, 7–9 and 17–20 were obtained from the USGS and California Geological Survey, Quaternary fault and fold database for the United States (<https://www.usgs.gov/natural-hazards/earthquake-hazards/faults>; last accessed 1 December 2019). Traces of surface ruptures from the 2019 Ridgecrest sequence shown in Figs 2, 7–9 and 17–20 were obtained from the Supplementary Material accompanying (Ponti *et al.* 2020). Locations of the  $M_w$  6.4 and  $M_w$  7.1 main shocks from Lomax (2020) were used in Figs 2 and 11–17. Data from the 3J network are described in Catchings *et al.* (2020). Data from the GS and ZY networks are described in Cochran *et al.* (2020). Data from the 3J and GS networks and can be accessed through the facilities of IRIS Data Services, and specifically the IRIS Data Management Center. Data

from the ZY network can be accessed through the Southern California Earthquake Data Center (Southern California Earthquake Center 2013).

## REFERENCES

- Akaike, H., 1974. A new look at the statistical model identification, *IEEE T. Automat. Contr.*, **19**(6), 716–723.
- Albuquerque Seismological Laboratory, United States Geological Survey, 1980. US Geological Survey Networks. International Federation of Digital Seismograph Networks, doi:10.7914/SN/GS.
- Barnhart, W.D., Hayes, G.P. & Gold, R.D., 2019. The July 2019 Ridgecrest, California, earthquake sequence: kinematics of slip and stressing in cross-fault ruptures, *Geophys. Res. Lett.*, **46**(21), 11 859–11 867.
- Ben-Zion, Y. & Zaliapin, I., 2019. Spatial variations of rock damage production by earthquakes in southern California, *Earth Planet. Sci. Lett.*, **512**, 184–193.
- Beyreuther, M., Barsch, R., Krischer, L., Megies, T., Behr, Y. & Wassermann, J., 2010. ObsPy: a Python toolbox for seismology, *Seismol. Res. Lett.*, **81**(3), 530–533.
- Brandenberg, S.J. *et al.*, 2020. Ground deformation data from GEER investigations of Ridgecrest earthquake sequence, *Seismol. Res. Lett.*, **91**(4), 2024–2034.
- Brietzke, G.B. & Ben-Zion, Y., 2006. Examining tendencies of in-plane rupture to migrate to material interfaces, *Geophys. J. Int.*, **167**(2), 807–819.
- California Institute of Technology, United States Geological Survey, 1926. Southern California Seismic Network, doi:10.7914/SN/CI.
- Catchings, R.D. *et al.*, 2020. Nodal seismograph recordings of the 2019 Ridgecrest earthquake sequence, *Seismol. Res. Lett.*, **91**(6), 3622–3633.
- Christensen, N.I., 1996. Poisson's ratio and crustal seismology, *J. geophys. Res.*, **101**(B2), 3139–3156.
- Cochran, E.S. *et al.*, 2020. The U.S. geological survey's rapid seismic array deployment for the 2019 Ridgecrest earthquake sequence, *Seismol. Res. Lett.*, **91**(4), 1952–1960.
- Donnellan, A., Lyzenga, G., Ansar, A., Goulet, C., Wang, J. & Pierce, M., 2020. Targeted high-resolution structure from motion observations over the  $M_w$  6.4 and 7.1 ruptures of the Ridgecrest earthquake sequence, *Seismol. Res. Lett.*, **91**(4), 2087–2095.
- DuRoss, C.B. *et al.*, 2020. Surface displacement distributions for the July 2019 Ridgecrest, California, earthquake ruptures, *Bull. seism. Soc. Am.*, **110**(4), 1400–1418.
- Fang, H., van der Hilst, R.D., de Hoop, M.V., Kothari, K., Gupta, S. & Dokmanić, I., 2020. Parsimonious seismic tomography with Poisson Voronoi projections: methodology and validation, *Seismol. Res. Lett.*, **91**(1), 343–355.
- Fielding, E.J., Liu, Z., Stephenson, O.L., Zhong, M., Liang, C., Moore, A., Yun, S.-h. & Simons, M., 2020. Surface deformation related to the 2019  $M_w$  7.1 and 6.4 Ridgecrest earthquakes in California from GPS, SAR Interferometry, and SAR Pixel offsets, *Seismol. Res. Lett.*, **91**(4), 2035–2046.
- Floyd, M., Funning, G., Fialko, Y., Terry, R. & Herring, T., 2020. Survey and continuous GNSS in the vicinity of the July 2019 Ridgecrest earthquakes, *Seismol. Res. Lett.*, **91**(4), 2047–2054.
- Harris, C.R. *et al.*, 2020. Array programming with NumPy, *Nature*, **585**(7825), 357–362.
- Hauksson, E., 2000. Crustal structure and seismicity distribution adjacent to the Pacific and North America plate boundary in southern California, *J. geophys. Res.*, **105**(B6), 13 875–13 903.
- Hauksson, E., Yang, W. & Shearer, P.M., 2012. Waveform relocated earthquake catalog for Southern California (1981 to June 2011), *Bull. seism. Soc. Am.*, **102**(5), 2239–2244.
- Hudnut, K.W. *et al.*, 2020. Airborne lidar and electro-optical imagery along surface ruptures of the 2019 Ridgecrest earthquake sequence, Southern California, *Seismol. Res. Lett.*, **91**(4), 2096–2107.
- Hunter, J.D., 2007. Matplotlib: a 2D graphics environment, *Comput. Sci. Eng.*, **9**(3), 90–95.

- Hutton, L.K. & Boore, D.M., 1987. The MI Scale in Southern California, *Bull. seism. Soc. Am.*, **77**(6), 2074–2094.
- Jin, Z. & Fialko, Y., 2020. Finite slip models of the 2019 Ridgecrest earthquake sequence constrained by space geodetic data and aftershock locations, *Bull. seism. Soc. Am.*, **110**(4), 1660–1679.
- Juarez, A. & Ben-Zion, Y., 2020. Effects of shallow-velocity reductions on 3D propagation of seismic waves, *Seismol. Res. Lett.*, **91**(6), 3313–3322.
- Lee, E.-J., Chen, P., Jordan, T.H., Maechling, P.B., Denolle, M.A.M. & Beroza, G.C., 2014. Full-3-D tomography for crustal structure in Southern California based on the scattering-integral and the adjoint-wavefield methods, *J. geophys. Res.*, **119**(8), 6421–6451.
- Lee, E.-J., Liao, W.-Y., Mu, D., Wang, W. & Chen, P., 2020a. GPU-accelerated automatic microseismic monitoring algorithm (GAMMA) and its application to the 2019 Ridgecrest earthquake sequence, *Seismol. Res. Lett.*, **91**(4), 2062–2074.
- Lee, E.-J., Mu, D., Wang, W. & Chen, P., 2020b. Weighted template-matching algorithm (WTMA) for improved foreshock detection of the 2019 Ridgecrest earthquake sequence, *Bull. seism. Soc. Am.*, **110**(4), 1832–1844.
- Lin, F.-C., Li, D., Clayton, R.W. & Hollis, D., 2013. High-resolution 3D shallow crustal structure in Long Beach, California: application of ambient noise tomography on a dense seismic array, *Geophysics*, **78**(4), Q45–Q56.
- Lin, G., 2020. Waveform cross-correlation relocation and focal mechanisms for the 2019 Ridgecrest earthquake sequence, *Seismol. Res. Lett.*, **91**(4), 2055–2061.
- Lin, G. & Shearer, P.M., 2009. Evidence for water-filled cracks in earthquake source regions, *Geophys. Res. Lett.*, **36**(17), L17315.
- Liu, M., Zhang, M., Zhu, W., Ellsworth, W.L. & Li, H., 2020. Rapid characterization of the July 2019 Ridgecrest, California, earthquake sequence from raw seismic data using machine-learning phase picker, *Geophys. Res. Lett.*, **47**(4), 1–9.
- Lomax, A., 2020. Absolute location of 2019 Ridgecrest seismicity reveals a shallow  $M_w$  7.1 hypocenter, migrating and pulsing  $M_w$  7.1 foreshocks, and duplex  $M_w$  6.4 ruptures, *Bull. seism. Soc. Am.*, **110**(4), 1845–1858.
- Louie, J.N., 2001. Faster, better: shear-wave velocity to 100 meters depth from refraction microtremor arrays, *Bull. seism. Soc. Am.*, **91**(2), 347–364.
- Maeda, N., 1985. A method for reading and checking phase time in auto-processing system of seismic wave data, *J. Seismol. Soc. Jpn.*, **38**(3), 365–379.
- Magen, Y., Ziv, A., Inbal, A., Baer, G. & Hollingsworth, J., 2020. Fault re-rupture during the July 2019 Ridgecrest earthquake pair from joint slip inversion of InSAR, optical imagery, and GPS, *Bull. seism. Soc. Am.*, **110**(4), 1627–1643.
- Mattioli, G.S. *et al.*, 2020. The GAGE data and field response to the 2019 Ridgecrest earthquake sequence, *Seismol. Res. Lett.*, **91**(4), 2075–2086.
- McKinney, W., 2010. Data structures for statistical computing in Python, in *Proceedings of the 9th Python in Science Conference*, pp. 56–61, doi:10.25080/Majora-92bf1922-00a.
- Perez, F. & Granger, B.E., 2007. IPython: a system for interactive scientific computing, *Comput. Sci. Eng.*, **9**(3), 21–29.
- Pierce, I., Williams, A., Koehler, R.D. & Chupik, C., 2020. High-resolution structure-from-motion models and orthophotos of the southern sections of the 2019  $M_w$  7.1 and 6.4 Ridgecrest earthquakes surface ruptures, *Seismol. Res. Lett.*, **91**(4), 2124–2126.
- Plesch, A., Shaw, J.H., Ross, Z.E. & Hauksson, E., 2020. Detailed 3D fault representations for the 2019 Ridgecrest, California, earthquake sequence, *Bull. seism. Soc. Am.*, **110**(4), 1818–1831.
- Ponti, D.J. *et al.*, 2020. Documentation of surface fault rupture and ground-deformation features produced by the 4 and 5 July 2019  $M_w$  6.4 and  $M_w$  7.1 Ridgecrest earthquake sequence, *Seismol. Res. Lett.*, **91**(5), 2942–2959.
- Qiu, H., Ben-Zion, Y., Catchings, R.D., Goldman, M.R., Allam, A.A. & Steidl, J.H., 2020. Detailed seismic imaging of the  $M_w$  7.1 Ridgecrest earthquake rupture zone from data recorded by dense linear arrays, Abstract for the annual meeting of the Southern California Earthquake Center.
- Ross, Z.E., Hauksson, E. & Ben-Zion, Y., 2017. Abundant off-fault seismicity and orthogonal structures in the San Jacinto fault zone, *Sci. Adv.*, **3**(3), e1601946.
- Ross, Z.E. *et al.*, 2019. Hierarchical interlocked orthogonal faulting in the 2019 Ridgecrest earthquake sequence, *Science*, **366**(6463), 346–351.
- Schuster, G.T., 2009. *Seismic Interferometry*, Cambridge Univ. Press.
- Scott, D., 2015. *Multivariate Density Estimation: Theory, Practice, and Visualization*, Wiley Series in Probability and Statistics, Wiley.
- Seyhan, E. & Stewart, J.P., 2014. Semi-empirical nonlinear site amplification from NGA-West2 data and simulations, *Earthq. Spectra*, **30**(3), 1241–1256.
- Shaw, J.H. *et al.*, 2015. Unified structural representation of the southern California crust and upper mantle, *Earth planet. Sci. Lett.*, **415**, 1–15.
- Shelly, D.R., 2020. A high-resolution seismic catalog for the initial 2019 Ridgecrest earthquake sequence: foreshocks, aftershocks, and faulting complexity, *Seismol. Res. Lett.*, **91**(4), 1971–1978.
- Shelly, D.R., Ellsworth, W.L. & Hill, D.P., 2016. Fluid-faulting evolution in high definition: connecting fault structure and frequency-magnitude variations during the 2014 Long Valley Caldera, California, earthquake swarm, *J. geophys. Res.*, **121**(3), 1776–1795.
- Small, P. *et al.*, 2017. The SCEC unified community velocity model software framework, *Seismol. Res. Lett.*, **88**(6), 1539–1552.
- Southern California Earthquake Center, 2013. *Southern California Earthquake Data Center*, doi:10.7909/c3wd3xh1.
- Steidl, J., Catchings, R. & Allam, A., 2019. RAMP deployment of 3C nodal for July Searles Valley 2019 Earthquake., International Federation of Digital Seismograph Networks, doi:10.7914/SN/3J.2019.
- Storn, R. & Price, K., 1997. Differential evolution — a simple and efficient heuristic for global optimization over continuous spaces, *J. Global Optim.*, **11**(4), 341–359.
- University of Nevada Reno, 1971. Nevada Seismic Network, International Federation of Digital Seismograph Networks, doi:10.7914/SN/NN.
- University of Nevada Reno, 1980. Southern Great Basin Network, International Federation of Digital Seismograph Networks, doi:10.7914/SN/SN.
- Virtanen, P. *et al.*, 2020. SciPy 1.0: fundamental algorithms for scientific computing in Python, *Nat. Methods*, **17**(3), 261–272.
- White, M. C.A., Ben-Zion, Y. & Vernon, F.L., 2019. A detailed earthquake catalog for the San Jacinto Fault-Zone region in Southern California, *J. geophys. Res.*, **124**, 6908–6930.
- White, M.C.A., Fang, H., Nakata, N. & Ben-Zion, Y., 2020. PyKonal: a Python package for solving the eikonal equation in spherical and Cartesian coordinates using the fast marching method, *Seismol. Res. Lett.*, **91**(4), 2378–2389.
- Xu, S. & Ben-Zion, Y., 2013. Numerical and theoretical analyses of in-plane dynamic rupture on a frictional interface and off-fault yielding patterns at different scales, *Geophys. J. Int.*, **193**(1), 304–320.
- Zhang, M., Ellsworth, W.L. & Beroza, G.C., 2019. Rapid earthquake association and location, *Seismol. Res. Lett.*, **90**(6), 2276–2284.
- Zhang, Q. & Lin, G., 2014. Three-dimensional  $V_p$  and  $V_p/V_s$  models in the Coso geothermal area, California: seismic characterization of the magmatic system, *J. geophys. Res.*, **119**(6), 4907–4922.
- Zigone, D., Ben-Zion, Y., Lehujeur, M., Campillo, M., Hillers, G. & Vernon, F.L., 2019. Imaging subsurface structures in the San Jacinto fault zone with high-frequency noise recorded by dense linear arrays, *Geophys. J. Int.*, **217**(2), 879–893.

## SUPPORTING INFORMATION

Supplementary data are available at *GJI* online.

**Figure S1.** Example results from checkerboard tests using a coarse checker-board.

**Figure S2.** Example results from checkerboard tests using an intermediate checkerboard.

**Figure S3.** Depth slices at 2 km below sea level for  $V_p$  models derived from different starting models.

**Figure S4.** Depth slices at 6 km below sea level for  $V_p$  models derived from different starting models.

**Figure S5.** Depth slices at 12 km below sea level for  $V_p$  models derived from different starting models.

**Figure S6.** Depth slices at 2 km below sea level for  $V_s$  models derived from different starting models.

**Figure S7.** Depth slices at 6 km below sea level for  $V_s$  models derived from different starting models.

**Figure S8.** Depth slices at 12 km below sea level for  $V_s$  models derived from different starting models.

**Figure S9.** Depth slices at 2 km below sea level for  $V_p/V_s$  models derived from different starting models.

**Figure S10.** Depth slices at 6 km below sea level for  $V_p/V_s$  models derived from different starting models.

**Figure S11.** Depth slices at 12 km below sea level for  $V_p/V_s$  models derived from different starting models.

Please note: Oxford University Press is not responsible for the content or functionality of any supporting materials supplied by the authors. Any queries (other than missing material) should be directed to the corresponding author for the paper.

## APPENDIX: DETECTING AND PICKING PHASE ARRIVALS

Bold-face lowercase letters represent vectors throughout this paper. Consider some time-series,  $\mathbf{x}$ , with  $n$  samples,  $\mathbf{x} = \langle x_0, x_1, \dots, x_{n-1} \rangle$ . Then  $\bar{x}$  denotes the mean value of  $\mathbf{x}$ ,  $\mathbf{x}[k] \equiv x_k$  denotes the sample with index  $k$ , and  $\mathbf{x}[i : j] \equiv \langle x_i, x_{i+1}, \dots, x_{j-1} \rangle$  denotes the segment of  $\mathbf{x}$  with indices running from  $i$  to  $j - 1$ . A superscript letter attached to the label of a time-series indicates that it corresponds to a particular data component—namely, Z, N or E—or phase—namely, P or S. Square brackets  $[\ ]$  enclose integer indices of time-series, parentheses  $(\ )$  enclose function arguments, and curly braces  $\{ \}$  indicate algebraic grouping.

### A1 Measuring $P$ -wave arrival times

Measuring the arrival times of the seismic phases used to locate events is the first critical step in the workflow we use to build an earthquake catalogue.  $S$ -wave arrival times are typically harder to measure than those for  $P$  waves because they arrive later and are interfered with by the  $P$ -wave coda, so we begin our processing by targeting  $P$ -wave arrivals. The existence of a  $P$  wave must first be detected before its arrival time can be measured; the following describes our approach to solving the two-part problem of detecting the existence of and measuring the arrival time of  $P$  waves.

A characteristic function (CF) based on three simple and intuitive statistics—the ratio of the signal variance in a short time window to the same in a longer window (STA/LTA), the signal kurtosis in a sliding window, and the ratio of the signal variance on the vertical channel to the mean of the same on the horizontal channels (V/H)—coupled with an adaptive threshold robustly detects  $P$ -wave arrivals (Fig. A1).

The STA/LTA,  $\mathbf{s}^P$ , is computed for vertical-component data,  $\mathbf{z}$ , using short- and long-term window lengths of 0.25 and 4 s, respectively:

$$s_i^P = \frac{\text{var}(\mathbf{z}[i - 0.25r : i])}{\text{var}(\mathbf{z}[i - 4r : i])},$$

in which  $r$  is the sampling rate and  $\text{var}(\cdot)$  is the sample variance of the argument:

$$\text{var}(\mathbf{x}) \equiv \frac{1}{n-1} \sum_{i=0}^{n-1} \{x_i - \bar{x}\}^2.$$

The sliding-window kurtosis for the vertical component,  $\mathbf{k}^P$ , is computed using a window length of 5 s:

$$k_i^P = \frac{\mu_4(\mathbf{z}[i - 5r : i])}{\{\text{var}(\mathbf{z}[i - 5r : i])\}^2},$$

in which  $\mu_4(\cdot)$  is the fourth central moment of the argument:

$$\mu_4(\mathbf{x}) \equiv \frac{1}{n-1} \sum_{i=0}^{n-1} \{x_i - \bar{x}\}^4.$$

The V/H ratio,  $\mathbf{v}$ , is computed using a window length of 0.5 s:

$$v_i = \frac{2 \cdot \text{var}(\mathbf{z}[i - 0.5r : i])}{\text{var}(\mathbf{n}[i - 0.5r : i]) + \text{var}(\mathbf{e}[i - 0.5r : i])},$$

in which  $\mathbf{n}$  and  $\mathbf{e}$  represent north–south and east–west component data, respectively.

Finally, the CF for detecting  $P$  waves,  $\mathbf{c}^P$ , is defined as the product of these three statistics:

$$c_i^P \equiv s_i^P k_i^P v_i,$$

and a threshold,  $t^P$ , is defined as six times the RMS of the CF in the preceding 5 s:

$$t_i^P \equiv 6 \times \sqrt{\frac{1}{5r} \sum_{j=0}^{5r} \{c_{i-j}^P\}^2}.$$

The algorithm registers a detection at every index where  $c_i^P > t_i^P$  and thins clusters by retaining only the detection with the highest signal-to-noise ratio (SNR) in each 1.5 s window. Then, the arrival time for each detected  $P$  wave is measured using the Akaike Information Criterion (AIC; Akaike 1974) by extracting a 3 s window centred on each detection and registering the sample index,  $i^*$ , corresponding to the global minimum of the AIC for that window:

$$i^* = \arg \min_i (i \log(\text{var}(\mathbf{z}[0 : i])) + \{n - i\} \log(\text{var}(\mathbf{z}[i : n]))).$$

### A2 Measuring $S$ -wave arrival times

Having determined the onset time of all candidate  $P$ -wave arrivals, the algorithm targets corresponding  $S$ -wave arrivals using a similar procedure, assuming, however, that at most one  $S$ -wave arrival exists in the time between two successive  $P$ -wave arrivals.

The STA/LTA in the  $S$ -wave case,  $\mathbf{s}^S$ , is defined using a 0.5 s short-term window and an expanding long-term window:

$$s_i^S = \frac{\text{var}(\mathbf{n}[i - 0.5r : i]) + \text{var}(\mathbf{e}[i - 0.5r : i])}{\text{var}(\mathbf{n}[0 : i]) + \text{var}(\mathbf{e}[0 : i])}.$$

The short-term window is longer for  $S$  waves than  $P$  waves because  $S$  waves tend to have longer duration. The expanding window used to define the long-term average serves to favor earlier arrivals over later when multiple high-energy signals occur within the segment of data being processed.

The kurtosis for the  $S$ -wave case,  $\mathbf{k}^S$ , is defined as the average kurtosis in a 0.5-s window across the horizontal channels:

$$k_i^S = \frac{1}{2} \left( \frac{\mu_4(\mathbf{n}[i - 5r : i])}{\{\text{var}(\mathbf{n}[i - 5r : i])\}^2} + \frac{\mu_4(\mathbf{e}[i - 5r : i])}{\{\text{var}(\mathbf{e}[i - 5r : i])\}^2} \right)$$

The V/H ratio is inverted when defining the  $S$ -wave characteristic function,  $\mathbf{c}^S$  to give

$$c_i^S \equiv \frac{s_i^S k_i^S}{v_i},$$

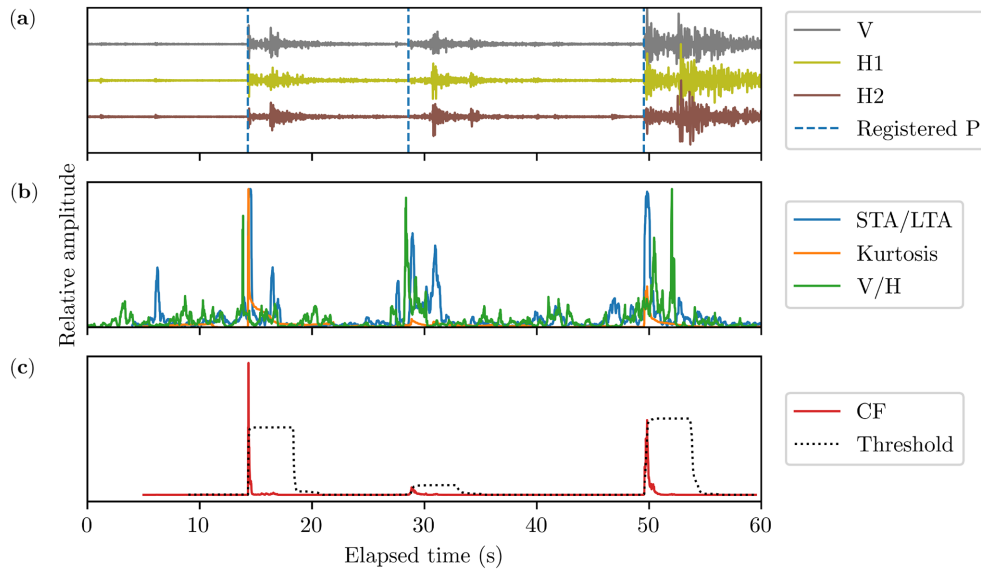


**Figure A1.** (a) 3C seismic waveform data with three registered *P*-wave arrivals (vertical dashed blue lines) and (b) derived statistics used to compute the (c) characteristic function (CF) and dynamic threshold.

and the index,  $i^* \equiv \arg \max_i c_i^S$ , coinciding with the maximum value of  $c^S$  provides an initial measurement of the arrival time. The AIC is then computed for a window centred on  $i^*$  with length equal to the

time interval between the preceding *P*-wave arrival and  $i^*$ . The index corresponding to the global minimum of the AIC is registered as the *S*-wave arrival time if the SNR at that index is greater than two.